NATIONAL UNIVERSITY OF SCIENCE
AND TECHNOLOGY POLITEHNICA
BUCHAREST
DOCTORAL SCHOOL OF
ELECTRICAL ENGINEERING

PhD THESIS

-SUMMARY-

STUDY OF CONTACT RESISTANCE IN AUTOMOTIVE LOW CURRENT CONNECTORS SUBJECTED TO AGING FACTORS

Scientific Coordinator,

Prof.Dr.Eng. Laurențiu Marius DUMITRAN

Author,

Eng. Gideon Gwanzuwang DANKAT

BUCHAREST

2023

CONTENTS

CHAPTER 1 – INTRODUCTION 4
CHAPTER 2 – LITERATURE REVIEW 5
2.1. Electrical Contacts 5
2.1.1. Aging of Electrical Contacts 6
2.1.1.1. Electrical Contacts Aging Mechanisms 6
2.2. Contact Resistance 6
2.2.1. Contact Interface 7
2.2.2. Measurement of Contact Resistance 7
CHAPTER 3 - NUMERICAL ANALYSIS OF LOW CURRENT CONTACTS 8
3.1. Model I: Model Development 8
3.1.1. Geometrical Model 8
3.1.2. Mathematical Model 9
3.1.2.1. Electrical Problem 9
3.1.2.2. Thermal Problem 10
3.2. Model II: Model Development 10
3.2.1. Geometrical Model 11
3.2.2. Mathematical Model 11
3.3. Model III: Model Development 11
3.3.1. Geometrical Model 12
3.3.2. Mathematical Model 12
3.4. Model IV: Model Development 12
3.4.1. Geometrical Model 13
3.4.2. Mathematical Model 13
CHAPTER 4 - ELECTRO-THERMAL COMPUTATION OF A LOW CURRENT CONTACT 14
4.1. Model I (Procedure and Objectives) 14
4.1.1. Results 14
4.1.2. Discussion 15
4.2. Model II (Procedure and Objectives) 15
4.2.1. Results 15
4.3. Contact Spots Multiphysics Analysis 17
4.3.1. Results 17
4.3.2. Discussion 19
CHAPTER 5 - ANALYTICAL AND NUMERICAL COMPUTATION OF ELECTRICAL RESISTANCE IN A LOW CURRENT MULTI-SPOT METALLIC CONTACT 19
5.1. Model III (Procedure and Objectives) 19
5.1.1. Results 19

5.1.2. Influence of Aging on Electrical Resistance (Model III) 20
5.1.2.1. Results 21
5.1.3. Model III Electro-Thermal Simulation (Procedure and Objectives) 22
5.1.3.1. Results 22
5.1.4. Discussion 23
5.2. Model IV (Procedure and Objectives) 24
5.2.1. Results 24
5.2.1.1. Contact Spot Thickness of 1 µm 24
5.2.1.2. Contact Spot Thickness of 10 µm 25
5.2.1.3. Contact Spot Thickness of 13 µm 26
5.2.1.4. Analytical Solution 26
5.2.2. Effect of Aging on Electrical Resistance (Model IV) 27
5.2.2.1. Results 27
5.2.2.1.1. Contact Spot Thickness of 1 µm 27
5.2.2.1.2. Contact Spot Thickness of 10 µm 27
5.2.2.1.3. Contact Spot Thickness of 13 µm 28
5.2.3. Model IV Electro-Thermal Simulation (Procedure and Objectives) 28
5.2.3.1. Results 29
5.2.3.1.1. Electro-Thermal Analysis (Contact Spot Thickness of 1 µm) 29
5.2.3.1.2. Electro-Thermal Analysis (Contact Spot Thickness of 10 µm) 30
5.2.3.1.3. Electro-Thermal Analysis (Contact Spot Thickness of 13 µm) 30
5.2.4. Discussion 31
CHAPTER 6 - EXPERIMENTAL VALIDATION OF CONTACT RESISTANCE CALCULATION 31
6.1. Samples 31
6.2. Experimental Setup and Measurements 32
6.3. Experimental Results 33
6.3.1. Contact Sample with ZrCu Alloy Spot Deposition of 1 µm 33
6.3.2. Contact Sample with ZrCu Alloy Spot Deposition of 10 µm 35
6.3.3. Contact Sample with ZrCu Alloy Spot Deposition of 13 µm 37
6.4. Discussion 38
GENERAL CONCLUSION, ORIGINAL CONTRIBUTIONS, AND FUTURE WORK 40
General Conclusion 40
Original Contributions 41
Future Work 42
REFERENCES 43

CHAPTER 1 – INTRODUCTION

The demand for safety, eco-friendliness, and software-enabled features in vehicles is increasing, leading automotive manufacturers to focus on electric vehicles (EVs). This has resulted in an increase in electric connectors in vehicles, with some already having over 300 connectors. [1.1]

This doctoral thesis aims to characterize the contact resistance of deteriorated electrical connections working under low-current situations, following the IEC-512-2-2a standard. The study involves developing different contact models and analyzing their degradation processes using Multiphysics numerical analysis using FEM in COMSOL Multiphysics. The research also evaluates the contact resistance influenced by various aging mechanisms, such as oxidation, temperature, contact force, and current. Physical electric contact samples are fabricated using the cathodic arc deposition method, and the degradation process is analyzed through an accelerated thermal aging process and resistance measurement using a four-point probe resistance measurement technique. The thesis comprises 6 chapters. The first two chapters present an introductory documentation of the proposed topic's importance and role, while chapters 3 - 6 deal with the description and results of the Numerical, analytical, and experimental studies conducted to achieve the proposed objectives of the thesis.

Chapter 1 presents a literature review of the proposed topic, highlighting the thesis's importance, main scope, and structure.

Chapter 2 of the thesis presents a theoretical framework on contact resistance, a key indicator of aging in electrical connectors. It provides in-depth documentation on its importance, measurement methods, and analytical methods. The chapter also discusses electrical contacts, their classifications, automotive connectors, and aging mechanisms that promote the aging of these contacts.

Chapter 3 presents the introductory part of numerical analysis (Multiphysics analysis). The chapter describes all the different models developed to achieve the objectives of the thesis. It begins with an introduction and the importance of numerical studies in the research field. A total of four numerical models were proposed (Models I - IV), which were considered to be in an electrokinetic regime. For each model considered for numerical degradation analysis, the model development, geometrical model, materials used, and the mathematical model applied was presented.

Chapter 4 deals with Multiphysics electro-thermal computation of a low current contact. It uses two models, denoted by Model I and Model II to analyze the impact of aging mechanisms on electrical contacts. The models consist of copper strips connected through circular contact spots. The chapter also examines interface spots using Model II to understand the impact of aging on electrical connector operation. The analysis starts with the electromagnetic problem and then the thermal problem, taking into account the Joule losses.

Chapter 5 examines numerical and analytical calculations for contact resistance in multi-spot low-current contact using other two models, denoted by Model III and Model IV. Model III, consisting of two copper disks connected by multiple points/spots, was numerically simulated and compared to Holm and Greenwood analytical models. Model IV, consisting of two copper electrodes in contact through multiple ZrCu spots with different spot thicknesses (ST: 1 μm, 10 μm, and 13 μm), was computed, considering contact load and comparing it to Lee and Drew analytical models. The results reveal differences between numerical and analytical models, the influence of aging on electrical resistance, the connection between contact resistance and contact load, and the influence of temperature on the contact models.

Chapter 6 presents the experimental part of the thesis, which was carried out by preparing some contact samples based on the structure and characteristics of Model IV presented in Chapter 3 and Chapter 5. The manufactured contact samples allow the resistance of the contact spots at the interface to be calculated as a function of the contact load. The sample is made up of ZrCu spots that were deposited on a copper-clad laminate (CCL). Samples with deposition thickness (DT) of 1 μm, 10 μm, and 13 μm were analyzed. The final section of the chapter addressed the variance in contact resistance against the contact load for different deposition thicknesses of ZrCu spots, and the results were compared to that of Model IV numerical model results to validate the model.

CHAPTER 2 – LITERATURE REVIEW

2.1. Electrical Contacts

Electrical contact is an important component in the automotive industry, involving the interaction of electrical and mechanical components to ensure the safe and uninterrupted flow of electrical current, facilitating the transmission of signals like information or power. However, various factors like temperature, humidity, and mechanical vibrations can impact the effectiveness of these connections.

Automotive connectors are essential in electric vehicle (EV) production, connecting electric systems and ensuring smooth operation. They consist of a male and female part and plastic housings, made from materials like copper, aluminum, and brass for high conductivity, strength, and corrosion resistance, and thermoplastics and thermoset sets for lightweight insulation.

2.1.1. Aging of Electrical Contacts

Electrical contacts are essential in electrical system design and construction, and their aging can significantly impact their functionality and dependability. Factors such as mechanical wear, corrosion, and high temperatures can cause degradation. The development of genuine and conducting contact regions controls the dependability of electrical connections [2.1]. These conductive areas depend on performance and design factors, such as contact coatings, materials, geometry, and contact interface topography.

2.1.1.1. Electrical Contacts Aging Mechanisms

***Corrosion*:** is a chemical or electrochemical reaction between a metal component and its environment that results in changes that cause the material to deteriorate, altering its properties and functionality. [2.2]

Fretting: in electrical contacts refers to the small-scale, repetitive motion or vibration that can occur between two contacting surfaces. This motion can cause the surfaces to rub against each other, leading to the formation of tiny particles or debris that can accumulate and interfere with the contact's electrical conductivity.

Thermal aging: Thermal aging of electrical links or connections pertains to a progressive deterioration of electrical connections that occur over time due to exposure to heat. When electrical contacts are exposed to high temperatures, such as those experienced in a typical automotive operating environment, several mechanisms can contribute to their aging.

2.2. Contact Resistance

Contact resistance in electrical contacts is influenced by various factors, including thermal effects, contact material composition, load/pressure, atmospheric conditions, and current. It occurs at the interface or contact point when conductors meet, causing voltage drops and localized heat, leading to thermal issues. The basic concept of contact resistance is illustrated in Fig. 2.1.

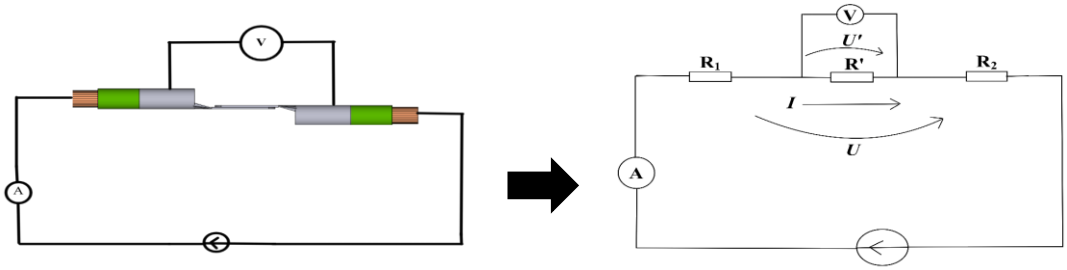

Fig. 2.1. Definition of contact resistance.

From Fig. 2.1 there is a decrease in voltage along the conductive part of the connector (i.e., $U \rightarrow U' < U$). This happens due to the transformation of energy in the form of voltage into other forms of energy like heat, light, etc.

2.2.1. Contact Interface

Solid surfaces are coarse, consisting of asperities with varying shapes and geometrical features. Contact between entities occurs at specific points due to structural irregularities, resulting in a minuscule portion of the visible contact region as demonstrated in Fig. 2.2.

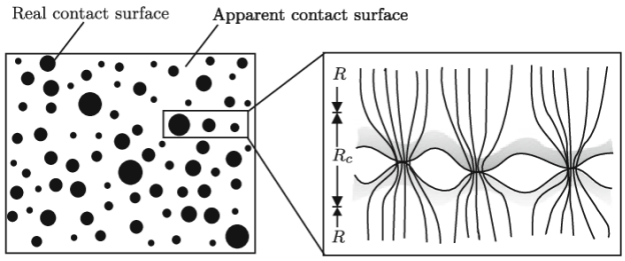

Fig. 2.2. A typical electrical interface diagram. [2.3]

2.2.2. Measurement of Contact Resistance

Contact resistance may be determined using a variety of techniques. Typically, these estimates are either determined by a contact surface model (numerical simulations), analytical methods or by precise experimental measurements. In this thesis the all three methods were utilized to evaluate the contact resistance. Holms (1) [2.4] and Greenwoods (2) [2.5] analytical model was used for analytical calculations whereas FEM in COMSOL Multiphysics and the 4-wire probe resistance measurement was employed for the numerical and experimental procedures correspondingly.

$$Rc = \frac{\rho}{2a} \tag{1}$$

$$R_{G1} = \frac{\rho}{2\sum a_i} + \frac{\rho}{\pi n^2} \sum_{i \neq j} \frac{1}{s_{ij}}. \tag{2}$$

CHAPTER 3 - NUMERICAL ANALYSIS OF LOW CURRENT CONTACTS

In this chapter, various simplified electrical contact models will be introduced in order to examine the deterioration process utilizing a Multiphysics analysis in COMSOL Multiphysics using the FEM. For simplification purposes, the a-spots were assumed to be circular. The analysis involves determining the temperature, electrical conductivity of the contact surfaces, and volume density of electric losses using an iterative technique. The electrical conductivity was calculated sequentially for each temperature value at each step till the newly determined temperature value matched the previous value.

3.1. Model I: Model Development

The investigation focuses on a basic electric copper contact in an air-filled box, estimating the distribution of electromagnetic field and temperature using the finite element approach (FEM) with low DC density. A 3D thermal-electrical coupled finite element simulation was used to examine temperature change, analyzing only the lower part of the contact surface.

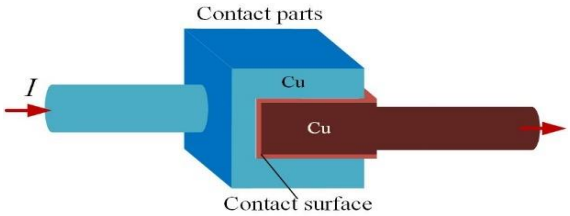

Fig. 3.1. Schematic view of the contact. [3.1]

3.1.1. Geometrical Model

The analysis focuses on the contact between two metal strips touching at 5 points, separated by a non-uniform oxide layer with varying electrical conductivity values. The asperities (contact points) are circular and vary in thickness from 10 μm to 50 μm. [3.1]

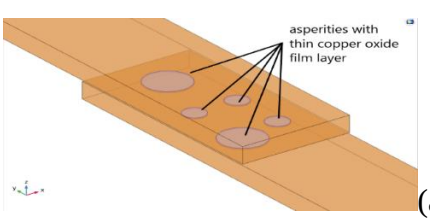

(a)

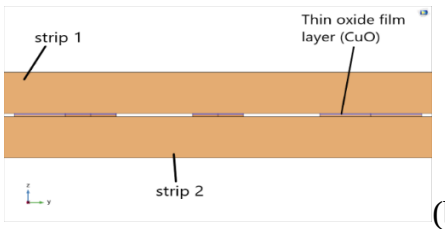

(b)

Fig. 3.2. Geometrical model (Model I): (a) the contact spots, (b) the thin oxide film layer. [3.1]

Table 3.1 shows the material properties used for the numerical analysis of Model I.

Table 3.1. Properties of copper and oxide - materials used for Model I [3.2, 3.3].

Property	***Expression***		***Unit***
	Copper	Oxide	
Electric conductivity	$5.96 \cdot 10^7$	$1 \cdot 10^3$	[S/m]
Thermal conductivity	400	33	[(W/ (m·K)]
Heat capacity at constant pressure	385	196	[J/(kg·K)]
Resistivity temperature coefficient	$3.9 \cdot 10^{-3}$	$3.9 \cdot 10^{-3}$	[1/K]

3.1.2. Mathematical Model

The combined electromagnetic (electrical) and thermal problem is investigated in the stationary electro-kinetic domain as part of the Multiphysics study.

3.1.2.1. Electrical Problem

The electromagnetic issue, assuming a stationary electro-kinetic regime, determines the distribution of an electric current of density $\boldsymbol{J}$ across a contact using three essential equations: electromagnetic induction law (3), electric conduction law (4), and electric charge conservation law (5). [3.1]

$$\text{rot } \boldsymbol{E} = 0, \tag{3}$$

$$\boldsymbol{J} = \sigma \cdot \boldsymbol{E} \tag{4}$$

$$\text{div } \boldsymbol{J} = 0, \tag{5}$$

where σ [S/m] represents the electrical conductivity and $\boldsymbol{E}$ [V/m] denotes the intensity of the electric field, it is assumed that the mediums are homogenous and isotropic, meaning that they do not change with temperature. As a result of electric potential V, the strength of the electrical field $\boldsymbol{E}$ can be evaluated:

$$\boldsymbol{E} = -\text{grad}V. \tag{6}$$

The boundary conditions are as follows:

Continuity:

$$\boldsymbol{n} \cdot (\boldsymbol{J}_1 - \boldsymbol{J}_2) = 0, \tag{7}$$

it asserts that the typical electrical current components are preserved and continuous through the internal boundary. The current densities $\boldsymbol{J}_1$ and $\boldsymbol{J}_2$ refer to the contact layer's opposing ends of the two copper strips.

Electric insulation:

$$\boldsymbol{n} \cdot \boldsymbol{J} = 0, \tag{8}$$

The volume density of electrical losses (Joule losses) caused by the electric current passing between copper strips and the contact interface is determined using the law of energy transformation:

$$P = \boldsymbol{J}\cdot\boldsymbol{E} = \sigma\boldsymbol{E}^2. \quad (9)$$

3.1.2.2. Thermal Problem

The thermal issue refers to the heating in contact due to resistive dissipation, defined by ambient temperature T_0, and is represented by a heat formula:

$$Q = \rho C_p \cdot dT/dt + \nabla\Psi, \quad (10)$$

in which ρ [kg/m^3] signifies the density, C_p [J/(kg·K)] represents the specific capacity for heat, Q the origin of heat and is equivalent to the volume density of electrical losses, and ψ [W/m^2] stands for the heat flux determined by the Fourier law:

$$\Psi = -\lambda \cdot \nabla T, \quad (11)$$

where the thermal conductivity, λ [W/(mK)] is assumed to be fixed i.e., it doesn't vary with temperature. Equation (10)'s starting condition is $T = T_0$ across all of the computation domain's points. Furthermore, continuity criteria (continuous heat flux) are enforced across every border separating the two distinct areas (subdomains) j and k:

$$\boldsymbol{n}\cdot(\lambda_j \cdot \nabla T - \lambda_k \cdot \nabla T) = 0, \quad (12)$$

where λ_j and λ_k represents the thermal conductivities associated with the j and k subdomains, respectively. Convection and radiation were disregarded in order to minimize the computation and duration of the simulation. [3.1]

3.2. Model II: Model Development

Model II has a similar geometry to Model I, with a discontinuous layer at the interface with lower electric conductivity. For numerical analysis, only the bottom portion of the contact surface labeled "2" is used. Model II consists of two overlapped copper strips, with 12 circular spots uniformly distributed at the interface, compared to Model I's 5 circular spots.

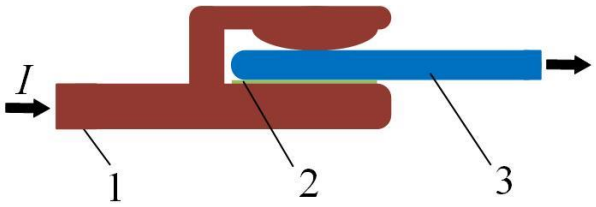

Fig. 3.3. Diagram of an electric contact: (1) & (3) contact components, and (2) the discontinuous layer at the interface. [3.4]

3.2.1. Geometrical Model

The copper strips are 10mm long, 1mm wide, and 0.2mm high, with a 3mm overlap. Twelve asperities connect the strips, with a thin oxide film layer. (Fig. 3.4). [3.4]

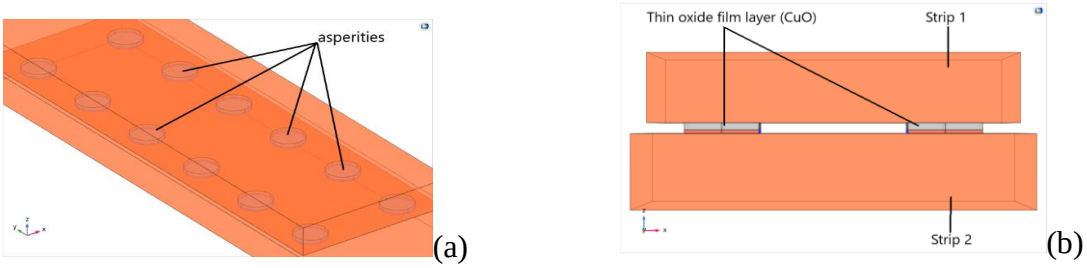

(a) (b)

Fig. 3.4. The two overlapping copper strips' geometry (model II): (a) the twelve points of contact, (b) the thin oxide layer at the contact region. [3.4]

Similar to the materials applied on Model I, copper was applied on the copper strips, and oxide was applied on the 12 asperities at the interface (see Table 3.1).

3.2.2. Mathematical Model

Model II, solved in the electrokinetic regime, assumes the electrical conductivity of the oxide layer on the contact surface (σ_O) to vary with temperature $\sigma_O(T)$. This differs from Model I, in which the electrical conductivity was considered invariant. The dependence between σ_O and oxide temperature was estimated using the following expression:

$$\sigma_O(T) = \{\rho_0[1 + \alpha\,(T\text{-}T_0)]\}^{-1}, \qquad (13)$$

where T is the temperature in ^{0}C, T_0 = 20 ^{o}C, $\rho_0 = 1\cdot10^{-3}$ Ωm, and the resistivity temperature coefficient is denoted by α ($\alpha = 3.90\cdot10^{-3}$).

3.3. Model III: Model Development

The numerical model in this case has a simplified form, consisting of two copper disks connected by several contact points as in Fig. 3.5. We will assume that the circular points are evenly dispersed over the entire surface. Unlike Models I and II, Model III has a disc shape and an insulating polyethylene layer for a more accurate analysis of the contact points.

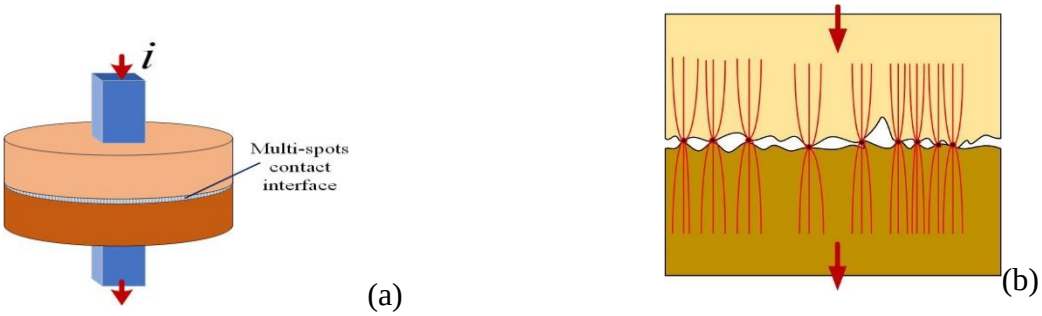

Fig. 3.5. A diagram of the contact setup: (a) Contact between copper disks; (b) current lines constricting as they pass across contact points. [3.5]

3.3.1. Geometrical Model

The study examined the contact points between two copper disks with 28 circular spots. The contact points have a radius of 0.2 mm, while the disks have a radius of 5 mm and a thickness of 1 mm. A 30 µm thick insulating layer confined current passage to these contact points. [3.5]

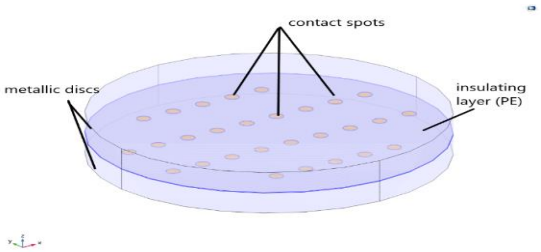

Fig. 3.6. Geometrical model (model III) showing the copper disks, contact spots, and the insulating layer. [3.5]

3.3.2. Mathematical Model

Model III, solved in the electro-kinetic regime, follows equations for electrical and thermal fields presented in Model I, with constant thermal and electrical conductivity and neglecting convection and radiation mechanisms.

3.4. Model IV: Model Development

The numerical model IV depicts two copper electrodes interacting through multiple ZrCu spots, with evenly distributed and equal dimensions. Although there may be limitations in numerical calculation performance, the ZrCu spots were modeled with reasonable dimensions, allowing for experimental studies to validate the model.

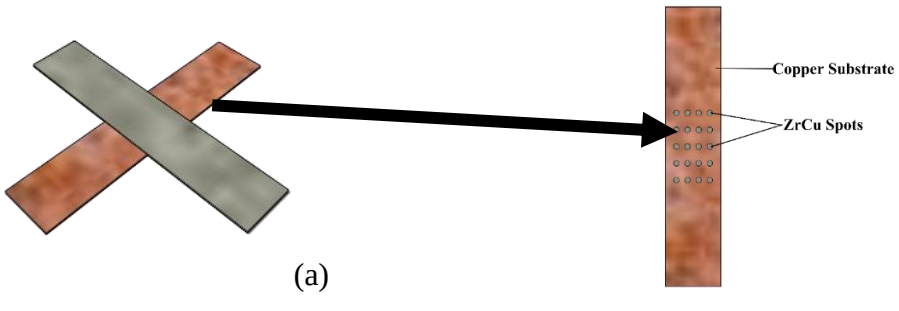

Fig. 3.7. The electrical contact setup schematic view: (a) the copper substrate, (b) the ZrCu spots at the interface.

3.4.1. Geometrical Model

The model consists of two 55 mm long and 17 mm wide electrodes connected by 36 circular ZrCu spots of 0.5 mm radius. Three different cases were analyzed where the thickness of these dots was considered as 1 μm, 10 μm, and 13 μm respectively (Fig. 3.8).

Fig. 3.8. Geometrical model (model IV) showing: (a) the copper electrodes, (b) the ZrCu spots at the interface.

3.4.2. Mathematical Model

Multiphysics model IV solves thermal, mechanical, and electromagnetic problems in the stationary electro-kinetic domain, using Cooper-Mikic-Yovanovich correlations for electrical contacts, ignoring radiation and convection mechanisms. [3.5-3.7]

$$\boldsymbol{n}\cdot\boldsymbol{J_1} = -h_c\,(V_1 - V_2), \tag{14}$$

$$\boldsymbol{n}\cdot\boldsymbol{J_2} = -h_c\,(V_2 - V_1), \tag{15}$$

in which $\boldsymbol{J}_1$ and $\boldsymbol{J}_2$ represent the current densities of both surfaces at the boundary layer between the upper electrode and the ZrCu contact spots, h_c signifies the Cooper-Mikic-Yovanovich relation connecting the contact load and asperities at the contact interface, and it is given by the following relation:

$$h_c = 1.25\sigma_{contact}\{(m_{asp} / \sigma_{asp}) \cdot (p / H_c)^{0.95}\} \tag{16}$$

where m_{asp} represents the asperities' average slope, σ_{asp} denotes the mean height of the surface roughness, p stands for the contact pressure, and H_c signifies the material's microhardness.

CHAPTER 4 - ELECTRO-THERMAL COMPUTATION OF A LOW CURRENT CONTACT

This chapter examines the interaction between electrical and thermal characteristics in contact models, aiming to compute the electro-thermal state of a low current contact using FEM numerical technique and COMSOL Multiphysics software.

4.1. Model I (Procedure and Objectives)

The study investigates the simplified contact Model I, analyzing temperature changes in contact zones as oxide film layer thicknesses and conductivities vary.

4.1.1. Results

Fig. 4.1 shows the temperature distribution for an injected current of 500 mA and the thermal conductivities of the copper strips, oxide layer, and air of 400 W/(m-K), 33 W/(m-K), and 0.0252 W/(m-K) respectively. From this, it can be seen that the peak temperature is 28°C due to the constriction of current paths and insulating oxide films.

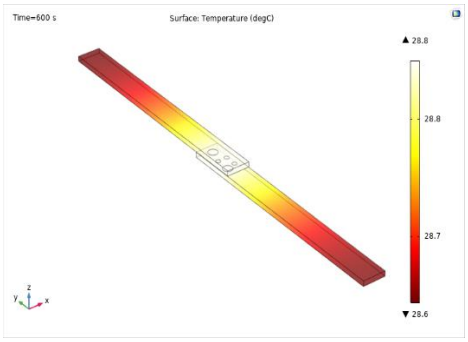

Fig. 4.1. Distribution of surface temperature at the copper strips and contact area.

Fig. 4.2 shows the temperature variation for different values of the electrical conductivity of the oxide layer at a constant current value of 100 mA (a) and the temperature variation for different values of the injected current at a constant electrical conductivity value of 10^3 S/m (b). [4.1]

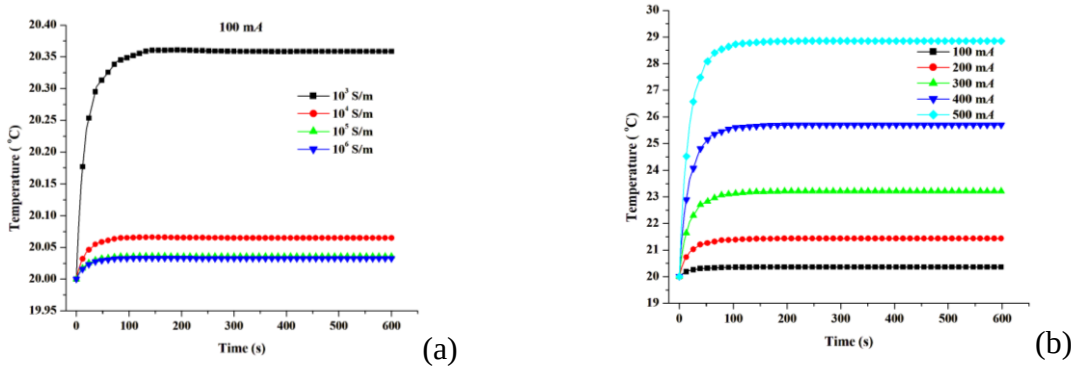

Fig. 4.2. Temperature changes with time: (a) for varied levels of the oxide film layer's electric conductivity; (b) for various supplied current levels.

For $\sigma_O = 10^3$ S/m and $\sigma_{Cu} = 5.96 \cdot 10^7$ S/m, Fig. 4.3 illustrates the change in contact temperature as the oxide film layer's thickness at the interface grows larger.

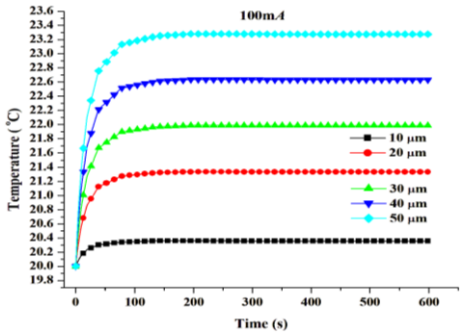

Fig. 4.3. Temperature variation with time for various oxide film layer thickness values at the contact interface for $\sigma_{Cu} = 5.96 \cdot 10^7$ S/m and $\sigma_O = 10^3$ S/m.

4.1.2. Discussion

A simplified electrical model with microscopic asperities was proposed for the computational investigation of temperature change in low-current electric connections influenced by oxidization. Results showed that temperature increases with injected current and thickness of oxide film, accelerating degradation of electric contacts over time.

4.2. Model II (Procedure and Objectives)

The electrothermal calculation procedure for Model II involves simulations for different oxide layer thicknesses and Multiphysics analysis of the points on the contact surface, focusing on the degradation of the insulating oxide layer.

4.2.1. Results

Fig. 4.4 shows the calculated temperature for an undegraded electrical contact. It can be seen that the maximum temperature reached in this case is 20.8°C. [4.2]

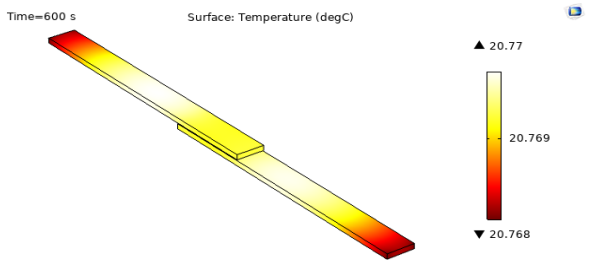

Fig. 4.4. The copper strip's temperature distribution for an unaged contact without the presence of oxide film layers at the interface.

Fig. 4.5 shows that a deteriorated contact with a 20 µm thick oxide layer at the contact area experiences a peak temperature of 54.3 ºC, resulting in increased electrical resistance and accelerated contact aging. [4.2]

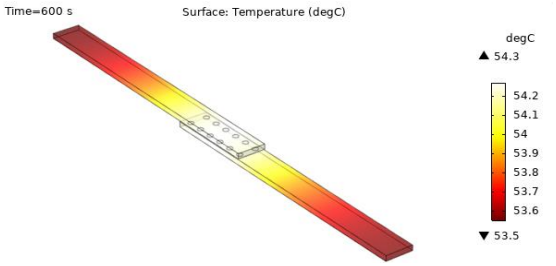

Fig. 4.5. The copper strip's temperature distribution having a thin film of oxide at the contact interface.

Fig. 4.6. illustrates the temperature changes as the oxide layer on the contact surface increases for a current of 200 mA (a) and as the applied current increases for an oxide layer thickness of 20 µm (b). [4.2]

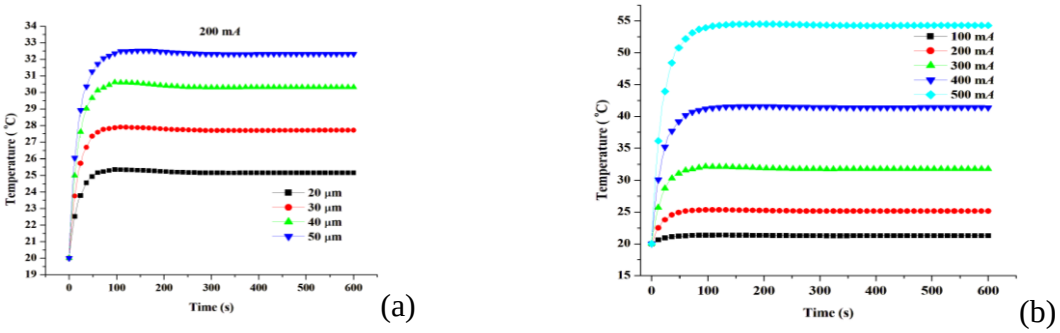

(a) (b)

Fig. 4.6. Temperature changes at the interface between the overlapping copper strips: (a) for varied oxide layer thickness; (b) for various applied current levels.

Fig. 4.7 illustrates the temperature-dependent variation of the oxide film's electrical conductivity situated at the point of contact. Chemical material oxides are typically

semiconductors, but the oxide layer at the interface is considered an aging product due to chemical reactions reducing contact electrical conductivity.

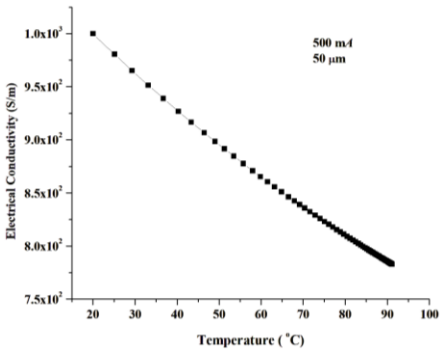

Fig. 4.7. Variations in the thin oxide film's electrical conductivity at the contact's interface with temperature (calculated using equation (13)).

4.3. Contact Spots Multiphysics Analysis

A series of simulations were considered for a Multiphysics analysis of contact spots at the interface, considering Model II with 12 circular spots covered by a discontinuous oxide layer. The oxide films had a thickness of 20 µm and were assigned different electrical conductivity values. All simulations were conducted at a 500 mA applied current.

4.3.1. Results

Fig. 4.8 shows the temperature distribution of 54.3 ^{o}C at the contact spots at the copper strip's interface, where all 12 oxide layers on the spots have electrical conductivity $\sigma = 1 \cdot 10^{3}$ S/m.

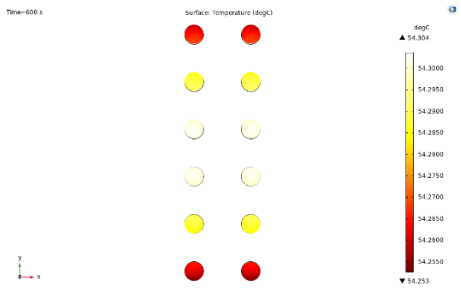

Fig. 4.8. The contact spots' surface temperature at the interface (all 12 spots with $\sigma = 1 \cdot 10^{3}$ S/m).

Considering the case where 3 points have electrical conductivity $1 \cdot 10^{-4}$ S/m, much lower than the other 9 contact points set at $1 \cdot 10^{3}$ S/m. Following the modifications we observe, as shown in Fig. 4.9a, that the temperature is concentrated on the points on the contact surface reaching values of about 66 ^{o}C, but without significant variations between the

12 points although the electrical conductivity is different for 3 of these points. The temperature concentration on the contact surface can also be seen in Fig. 4.9b, represented by a 3D plot of the temperature distribution for the entire medium from the air-filled box to the contact surface. In this type of representation the difference between the contact surface and the rest of the medium is much more visible, with temperatures ranging from 20 ^{o}C to 66 ^{o}C, and the temperature distribution at the points is highlighted, 3 of which have a flat surface due to higher resistance and lower current density.

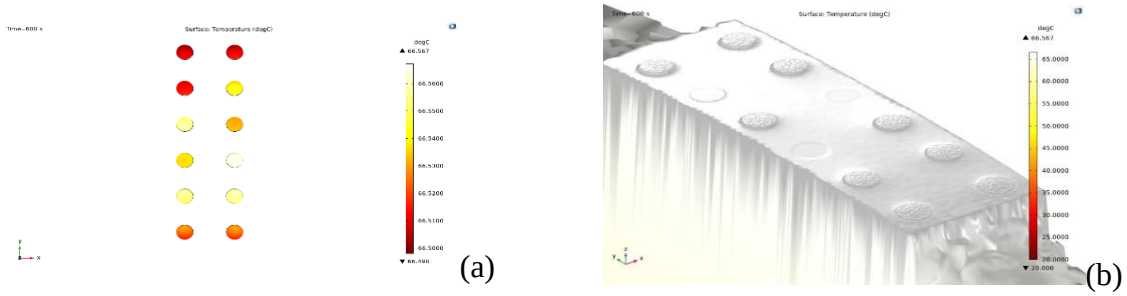

Fig. 4.9. Temperature distribution: a) the contact spots' surface b) the contact spots' height plot (3 contact spots with $\sigma = 1 \cdot 10^{-4}$ S/m and 9 contact spots with $\sigma = 1 \cdot 10^{3}$ S/m).

Fig. 4.10 shows the temperature variation when changing the number of contact points having a lower value of electrical conductivity, equal to $1 \cdot 10^{-4}$ S/m. It can be seen that the surface temperature increases with the number of points having lower conductivity.

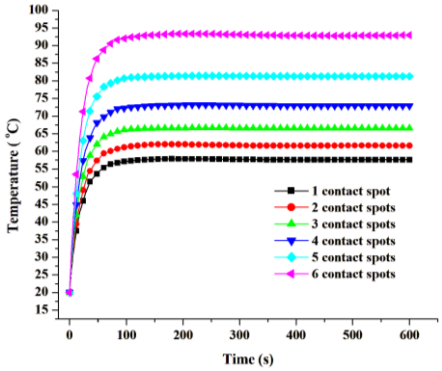

Fig. 4.10. The Copper strip temperature variation for various oxide layer electrical conductivity values at the contact's interface.

In the worst-case scenario, where 10 of the 12 contact points on the surface have a lower electrical conductivity value equal to $1 \cdot 10^{-4}$ S/m, Fig. 4.11a) and b) show a maximum temperature of 307 ^{o}C. Such a high temperature favors damage and eventually leads to electrical contact breakage. The 3D graph shows that the points with a conductivity of $1 \cdot 10^{3}$ S/m are more elevated, indicating a higher temperature value.

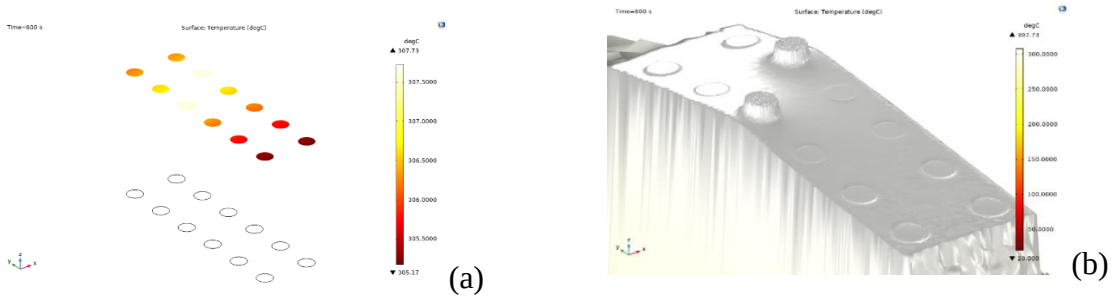

(a) (b)

Fig. 4.11. Temperature distribution at the: (a) contact zone of the copper strips, (b) height plot of the contact spots.

4.3.2. Discussion

A study on the impact of aging on low-current contacts using copper strips showed that aging mechanisms, such as oxides, contribute to the degradation and a significant increase in temperature at the contact. Electrical conductivity decreases with temperature, indicating increased resistance. High-temperature values are problematic as they can accelerate degradation and cause fire outbreaks.

CHAPTER 5 - ANALYTICAL AND NUMERICAL COMPUTATION OF ELECTRICAL RESISTANCE IN A LOW CURRENT MULTI-SPOT METALLIC CONTACT

This chapter explores the calculation of electrical resistance in low-current contacts using analytical and numerical methods. It discusses the impact of resistance on contact degradation and the tools used for both analytical and numerical computations.

5.1. Model III (Procedure and Objectives)

Model III consists of copper metal discs with multiple contact points to which a DC of 200 mA has been applied, and an electromagnetic field distribution was estimated using FEM in COMSOL Multiphysics. Contact resistance was evaluated using voltage drop across contact spots. Analytical models were compared to numerical models for contact point radii ranging from 0.1 mm to 0.5 mm. [5.1]

5.1.1. Results

Fig 5.1 depicts the estimated voltage for a 200 mA supplied current (J = 2.546·10^{-3} A/mm^2), copper disks and contact spots having a resistivity $\rho_{Cu} = \rho_{Cs}$ = 1.72·10^{-8} Ω·m. The peak voltage measured is around 0.4 μV.

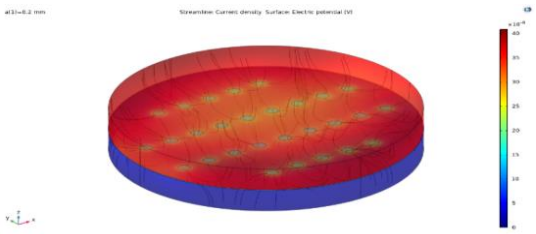

Fig. 5.1. Calculated voltage for 200 mA applied current.

Fig 5.2 depicts the voltage drop for various contact point radii (a = 0.1 mm - 0.5 mm). [5.1]

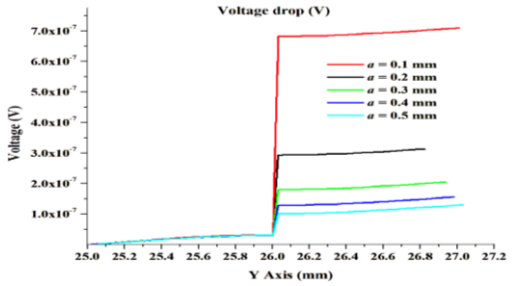

Fig. 5.2. The drop in voltage for various contact point radius (a = 0.1 mm / 0.5 mm) parameters.

The contact resistance data, estimated using Greenwood's and Holm's equations, and numerical simulation values are shown in Fig 5.3. The contact resistance decreases as contact point radius increases in all three scenarios. [5.2]

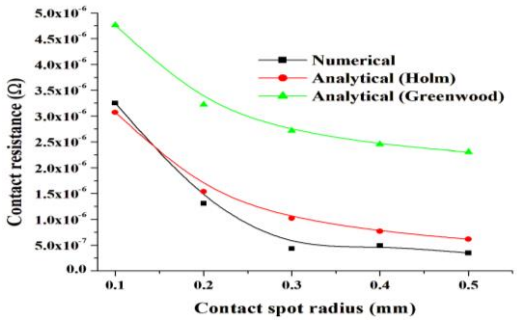

Fig. 5.3. Calculation of contact resistance with analytical data from Holm (●) and Greenwood (▲) and numerical analysis (■) for $\rho_{Cu} = \rho_{Cs} = 1.72 \cdot 10^{-8}$ Ω·m.

5.1.2. Influence of Aging on Electrical Resistance (Model III)

To investigate the effect of aging upon electrical resistance, Model III's circular contact points were given a resistivity higher than that of the two metallic copper disks, and the electrical resistance was calculated analytically (Holm and Greenwood model) and numerically using FEM in COMSOL Multiphysics.

5.1.2.1. Results

In Fig 5.4, two sub-figures (a) and (b) depict the resistance of the contact estimated for various contact spot resistivity values, $\rho_{Cs} = 1.72 \cdot 10^{-6}$ Ωm and $\rho_{Cs} = 1.72 \cdot 10^{-4}$ Ωm, while maintaining a constant copper disk resistivity, $\rho_{Cu} = 1.72 \cdot 10^{-8}$ Ωm. [5.2]

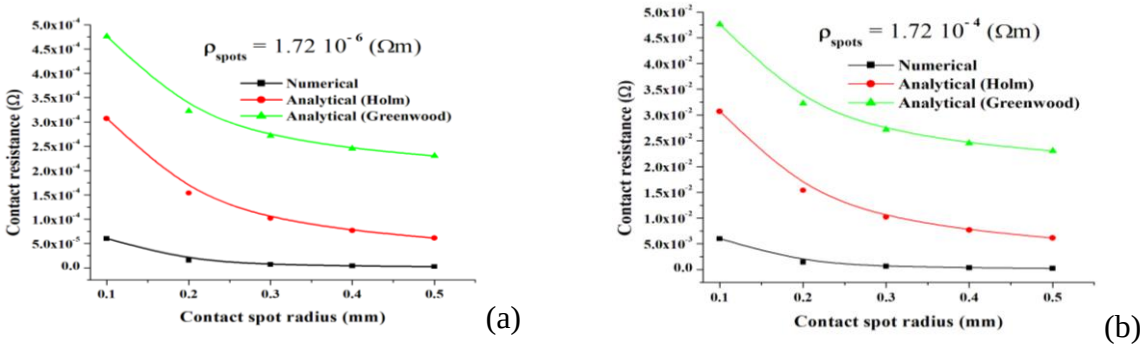

Fig. 5.4. Contact resistance displaying analytical parameters of Holm and Greenwood models and numerically computed values for $\rho_{Cu} = 1.72 \cdot 10^{-8}$ Ω·m and (a) $\rho_{Cs} = 1.72 \cdot 10^{-6}$ Ω·m; (b) ρCs = $1.72 \cdot 10^{-4}$ Ω·m.

The data presented in Fig. 5.5 exhibits the contact resistance computed using copper disks resistivity of $\rho_{Cu} = 1.72 \cdot 10^{-8}$ Ωm and contact spots resistivity of (a) $\rho_{Cs} = 1.72 \cdot 10^{2}$ Ωm and (b) $\rho_{Cs} = 1.72 \cdot 10^{4}$ Ωm. [5.2]

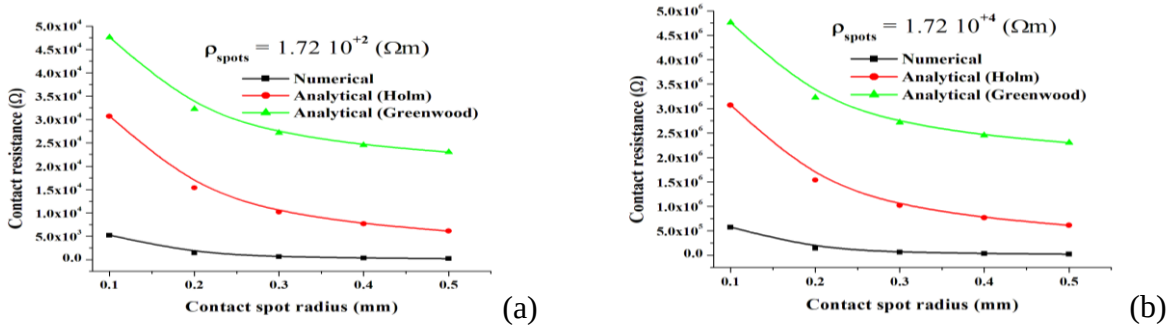

Fig. 5.5. Contact resistance parameters for the Holm and Greenwood theories and the numerical computations for $\rho_{Cu} = 1.72 \cdot 10^{-8}$ Ω·m and: (a) $\rho_{Cs} = 1.72 \cdot 10^{+2}$ Ω·m; (b) $\rho_{Cs} = 1.72 \cdot 10^{+4}$ Ω·m.

The contact resistance data derived only by numerical computation are displayed in Fig. 5.6. The study assumed a constant resistivity of $\rho_{Cu} = 1.72 \cdot 10^{-8}$ Ωm for the copper disks, while the 28 contact spots had resistivities of $\rho_{Cs} = 1.72 \cdot 10^{-6}$ Ωm (■), $\rho_{Cs} = 1.72 \cdot 10^{-4}$ Ωm (●), and $\rho_{Cs} = 1.72 \cdot 10^{-2}$ Ω·m (▲). Additionally, the study examined the scenario where the

28 contact spots had resistivities ranging between $1.72 \cdot 10^{-6}$ Ω·m to $1.72 \cdot 10^{+6}$ Ω·m (▼). [5.2].

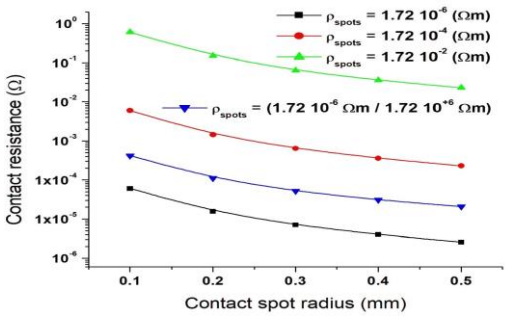

Fig. 5.6. The contact resistance parameters for the numerical model acquired for ρ_{Cu} = $1.72 \cdot 10^{-8}$ Ωm; ρ_{Cs} = $1.72 \cdot 10^{-6}$ Ωm; ρ_{Cs} = $1.72 \cdot 10^{-4}$ Ωm; ρ_{Cs} = $1.72 \cdot 10^{-2}$ Ωm, and, respectively, ρ_{Cs} = ($1.72 \cdot 10^{-6}$ Ωm/$1.72 \cdot 10^{+6}$ Ωm).

5.1.3. Model III Electro-Thermal Simulation (Procedure and Objectives)

The thermal analysis of Model III was conducted using FEM in COMSOL Multiphysics, focusing on material characteristics at contact points/spots. Due to the analytical nature of Holm and Greenwood equations and the difficulty in accurate thermal analysis, this section focuses on numerically computed contact resistance in Fig. 5.3.

5.1.3.1. Results

The steady-state distribution of temperature corresponding to the contact model is displayed in Fig 5.7. for a 200-mA current, T_0 = 20 °C, a = 0.1 mm, ρ_{PE} = $1 \cdot 10^{+17}$ Ωm, ρ_{Cu_disc}= $1.72 \cdot 10^{-8}$ Ωm, and 28 contact spots with a resistivity of (a) ρ_{Cu_spots} =$1.72 \cdot 10^{-8}$ Ωm and (b) ρ_{Cu_spots} =$1 \cdot 10^{-3}$ Ωm.

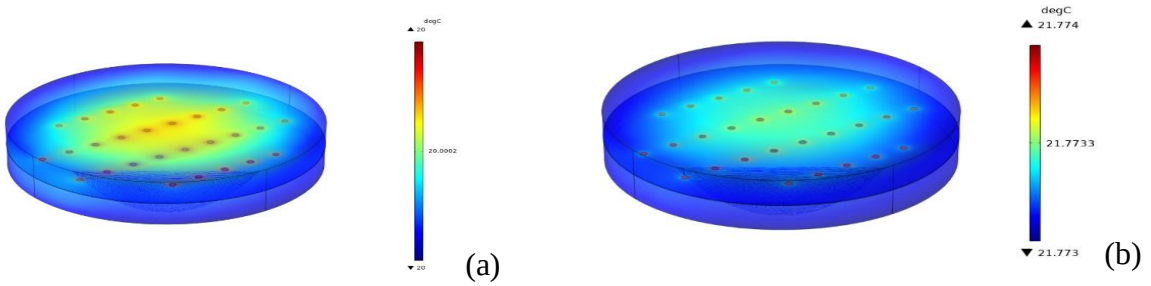

Fig. 5.7. Temperature distribution ρ_{Cu_disk} = $1.72 \cdot 10^{-8}$ Ωm and 28 point/spot of contact with (a) ρ_{Cu_spots} = $1.72 \cdot 10^{-8}$ Ωm; (b) ρ_{Cu_spots} = $1.72 \cdot 10^{-3}$ Ωm.

The stable state temperature range of the contact model is displayed in Fig. 5.8 for a 200-mA supplied current, T_0 = 20 °C, ρ_{PE} = $1 \cdot 10^{+17}$ Ωm, ρ_{Cu_disk}= $1.72 \cdot 10^{-8}$ Ωm, a = 0.1 mm

and three contact spots with a resistivity of (a) ρ_{Cu_spots} =1·10^{-3} Ωm and (b) (1·10^{-1} Ωm, 1·10^{-3} Ωm, and 1·10^{-2} Ωm consecutively).

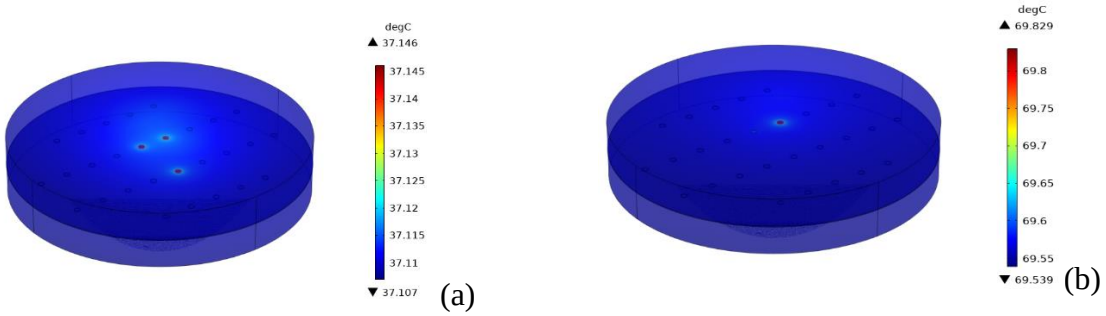

Fig. 5.8. Temperature distribution for ρ_{Cu_disk} = 1.72·10^{-8} Ωm and 3 spot of contact with (a) ρ_{Cu_spots}=1·10^{-3} Ωm; (b) ($\rho_{Cu\text{-}spots1}$=1·10^{-1} Ωm, $\rho_{Cu\text{-}spots2}$=1·10^{-3} Ωm, $\rho_{Cu\text{-}spots3}$=1·10^{-2} Ωm, $\rho_{Cu\text{-}disk}$ =1.72·10^{-8} Ωm).

The temperature changes of all four instances depicted in Figs. 5.7 and 5.8 are depicted in Fig. 5.9.

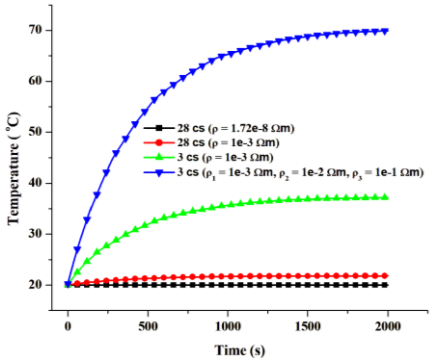

Fig. 5.9. The changes in temperature over time determined in the four situations.

Fig. 5.7a shows no significant temperature change, but Figs. 5.7b, 5.8a, and 5.8b show maximum temperatures of 21 ºC, 37 ºC, and 69 ºC respectively, indicating that decreasing electrically conducting areas in the contact interface increases the temperature. [5.3]

5.1.4. Discussion

The study analyzed contact resistance values for copper disks interacting through 24 circular contact spots. Greenwood and Holm methods were used, with numerical values consistently lower than analytical models. The numerical value was 80% and 10% different from Greenwood and Holm's values for spot radii of 0.1 mm, respectively. Holm achieved double the numerical value for 0.5 and 0.3 mm, while Greenwood achieved 7 times greater outcomes. The large number of contact areas with high resistivity increases the contact resistance of the connector due to impurities on the contact surface of the connector. This is

common in deteriorated electrical connections and also observed in the works of Shibata et al. [5.4]

5.2. Model IV (Procedure and Objectives)

Model IV uses copper electrodes connected by ZrCu spots, with a 10 mA low-level DC. The electric field distribution is estimated using electrical contact node FEM in COMSOL Multiphysics for spot radius of 0.5 mm and thicknesses of 1 µm, 10 µm, and 13 µm respectively, considering normal contact loads of 500, 700, 800, 820, 900, and 920 grams. The contact resistance was calculated for each spot thickness and an aging analysis was conducted by increasing the resistivity of ZrCu spots. To calculate the contact resistance analytically, Lee and Drew's model was used [5.5], expressing it as a result of the force applied:

$$R_c = [\rho^2 \eta \pi H/4F]^{1/2} \quad (17)$$

where ρ is the conducting metal's resistivity, η is an actual coefficient for the metal's surface's cleanliness state (≈ 1), H denotes the metal's hardness, and exerted force is denoted by F.

5.2.1. Results

5.2.1.1. Contact Spot Thickness of 1 µm

Fig. 5.10 demonstrates the voltage calculated with a 10 mA input current, $\rho_{ZrCuspots} = 1 \cdot 10^{-6}$ Ωm, $\rho_{electrodes} = 1.72 \cdot 10^{-8}$ Ωm, the mean height of asperities and surface roughness $\sigma_{asp} = 0.3$ µm and the mean slope of surface roughness asperities $m_{asp} = 0.4$ taking into consideration a spot thickness of 1 µm.

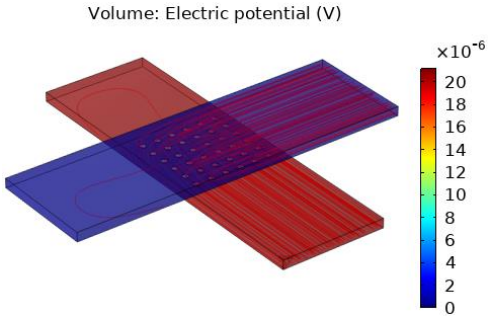

Fig. 5.10. Computed voltage for 10 mA input current (ST: 1 µm).

Fig. 5.11 displays the outcome of the resistance of the contact simulated as a result of added load when the electrical contact is considered unaged.

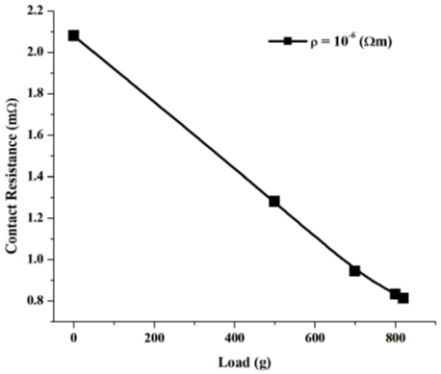

Fig. 5.11. Computed contact resistance versus contact load: $\rho_{electrodes} = 1.72 \cdot 10^{-8}$ Ωm and $\rho_{ZrCuspots} = 1 \cdot 10^{-6}$ Ωm (ST: 1 µm).

5.2.1.2. Contact Spot Thickness of 10 µm

Figure 5.12 depicts the voltage calculated for a 10 mA supplied current, $\rho_{ZrCuspots} = 1 \cdot 10^{-6}$ Ωm, $\rho_{electrodes} = 1.72 \cdot 10^{-8}$ Ωm, the mean height of asperities and surface roughness σ_{asp} = 0.6 µm and the mean slope of surface roughness asperities m_{asp} = 0.4 taking into consideration a spot thickness of 10 µm.

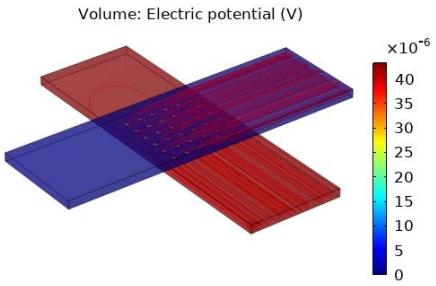

Fig. 5.12. Computed voltage for 10 mA input current (ST: 10 µm).

Figure 5.13 depicts the contact resistance determined for an unaged electrical contact as a result of contact load.

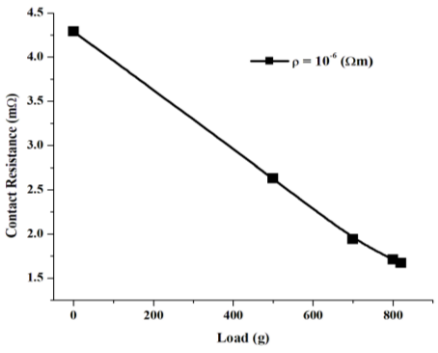

Fig. 5.13. Computed contact resistance versus contact load: $\rho_{electrodes} = 1.72 \cdot 10^{-8}$ Ωm and $\rho_{ZrCuspots} = 1 \cdot 10^{-6}$ Ωm (ST: 10 µm).

5.2.1.3. Contact Spot Thickness of 13 µm

Fig. 5.14 demonstrates the voltage calculated with a 10 mA input current, ρZrCuspots = $1 \cdot 10^{-6}$ Ωm, ρelectrodes = $1.72 \cdot 10^{-8}$ Ωm, the mean height of asperities and surface roughness σ_{asp} = 1 µm and the mean slope of surface roughness asperities m_{asp} = 0.4 taking into consideration a spot thickness of 13 µm.

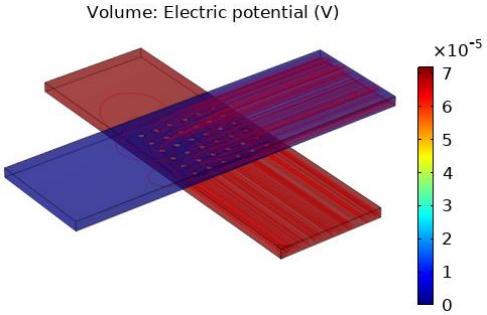

Fig. 5.14. Computed voltage for an injected current of 10 mA (ST: 13 µm)

Figure 5.15 depicts the contact resistance determined for an unaged electrical contact as a result of contact load.

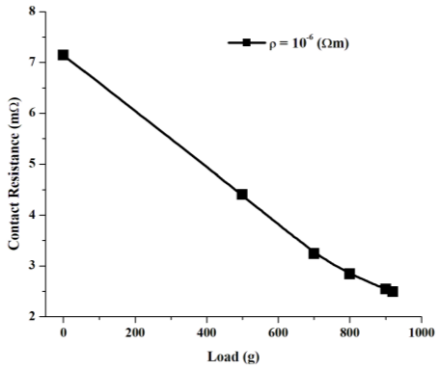

Fig. 5.15. Computed contact resistance versus contact load: $\rho_{electrodes} = 1.72 \cdot 10^{-8}$ Ωm and $\rho_{ZrCuspots} = 1 \cdot 10^{-6}$ Ωm (ST: 13 µm).

5.2.1.4. Analytical Solution

The contact resistance evaluated using the analytical expression in equation (17) is presented in Fig. 5.16.

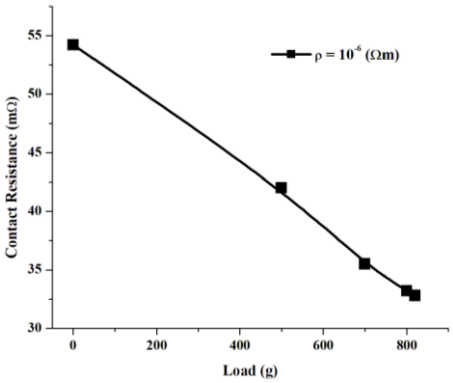

Fig. 5.16. Calculation of contact resistance with analytical values from equation (17).

5.2.2. Effect of Aging on Electrical Resistance (Model IV)

The study examines the impact of aging on the electrical resistance in model IV, considering a higher order resistivity (10^{-5}, 10^{-4}, 10^{-3}, 10^{-2} Ωm) of the ZrCu spots, the resistivity of the copper electrodes remaining the same ($1.72 \cdot 10^{-8}$ Ωm), for a current of 10 mA. The contact resistance following the application of a load was studied for all thicknesses of 1 µm, 10 µm, and 13 µm, respectively.

5.2.2.1. Results

5.2.2.1.1. Contact Spot Thickness of 1 µm

Contact resistance versus contact load is shown in Fig. 5.17 for various resistivity values of the ZrCu spots at the interface with a thickness of 1 µm for a supplied current of 10 mA.

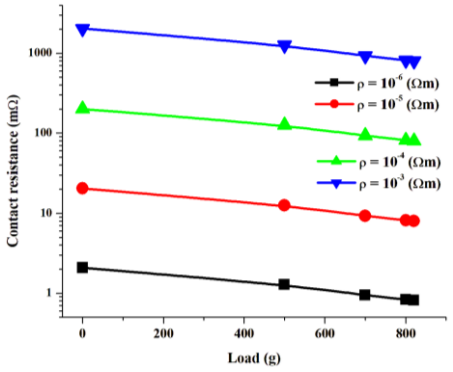

Fig. 5.17. Contact resistance showing values calculated for $\rho_{Zrcuspots} = 1 \cdot 10^{-6}$ Ω·m; $\rho_{Zrcuspots} = 1 \cdot 10^{-4}$ Ω·m; $\rho_{Zrcuspots} = 1 \cdot 10^{-5}$ Ω·m; $\rho_{Zrcuspots} = 1 \cdot 10^{-3}$ Ω·m and $\rho_{electrodes} = 1.72 \cdot 10^{-8}$ Ω·m (ST: 1 µm).

5.2.2.1.2. Contact Spot Thickness of 10 µm

Figure 5.18 displays the estimated contact resistance for various ZrCu spot resistivity values with a thickness of 10 µm for a 10mA applied current.

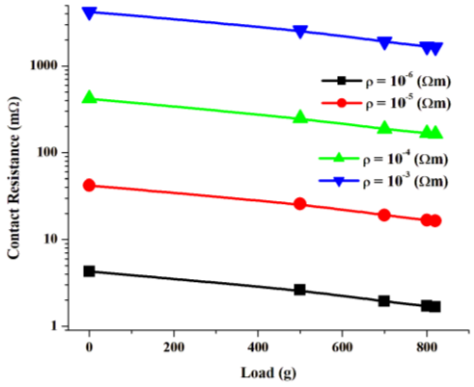

Fig. 5.18. Contact resistance showing values calculated $\rho_{Zrcuspots} = 1 \cdot 10^{-6}$ Ω·m; $\rho_{Zrcuspots} = 1 \cdot 10^{-4}$ Ω·m; $\rho_{Zrcuspots} = 1 \cdot 10^{-5}$ Ω·m; $\rho_{Zrcuspots} = 1 \cdot 10^{-3}$ Ω·m and $\rho_{electrodes} = 1.72 \cdot 10^{-8}$ Ω·m (ST: 10 µm).

5.2.2.1.3. Contact Spot Thickness of 13 µm

The contact resistance evaluated for different values of ZrCu spots with a spot thickness of 13 µm for an injected current of 10 mA is represented in Fig. 5.19.

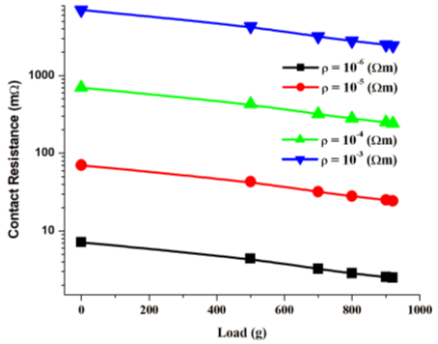

Fig. 5.19. Contact resistance showing values calculated for $\rho_{Zrcuspots} = 1 \cdot 10^{-6}$ Ω·m; $\rho_{Zrcuspots} = 1 \cdot 10^{-4}$ Ω·m; $\rho_{Zrcuspots} = 1 \cdot 10^{-5}$ Ω·m; $\rho_{Zrcuspots} = 1 \cdot 10^{-3}$ Ω·m and $\rho_{electrodes} = 1.72 \cdot 10^{-8}$ Ω·m (ST: 13 µm).

5.2.3. Model IV Electro-Thermal Simulation (Procedure and Objectives)

The electromagnetic and thermal problems of Model IV were analyzed using the volume density of electrical losses from the electromagnetic simulation, using the electrical contact node in the FEM COMSOL Multiphysics package. Contact configurations like Model IV experience varying applied loads resulting in deformations. These changes affect the contact characteristics and uniformity of the applied load. Aging analysis is performed for each thickness of the contact points by increasing their resistivity value.

5.2.3.1. Results

The calculated temperature for 10 mA of current, $\rho_{ZrCuspots} = 1 \cdot 10^{-6}$ Ωm, $\rho_{electrodes} = 1.72 \cdot 10^{-8}$ Ωm, and spot thickness ST: 13 µm, at T_0 = 20 ˚C is shown in Fig. 5.20. At normal operational conditions when the contact is considered unaged, the temperature distribution simulated shows no significant rise compared to the initial temperature T_0. The same conclusion was reached for all contact point thicknesses (1 µm, 10 µm, 13 µm).

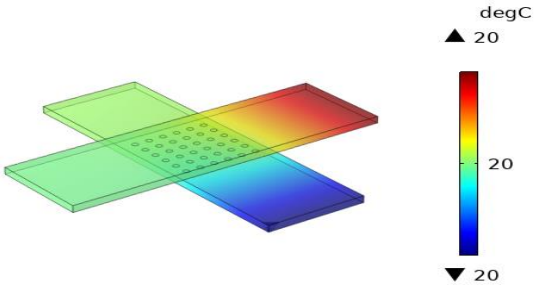

Fig. 5.20. Temperature distribution for a spot thickness of 13 µm ($\rho_{Zrcuspots} = 1.72 \cdot 10^{-6}$ Ω·m; $\rho_{electrodes} = 1.72 \cdot 10^{-8}$ Ω·m).

5.2.3.1.1. Electro-Thermal Analysis (Contact Spot Thickness of 1 µm)

In a case where the ZrCu spots at the interface degrade and become more resistive to the passage of current, or they go through some changes whereby some spots become insulated, the steady-state temperature distribution against the contact load for a spot thickness of 1 µm is illustrated in Fig. 5.21 for: (a) 36 spots ($\rho_{ZrCuspots} = 1 \cdot 10^{-2}$ Ωm); (b) only 4 spots conducting ($\rho_{ZrCuspots} = 1 \cdot 10^{-2}$ Ωm); (c) 4 spots (2 spots ($\rho_{ZrCuspots} = 1 \cdot 10^{-2}$ Ωm) and 2 spots ($\rho_{ZrCuspots} = 1 \cdot 10^{-1}$ Ωm)), with the resistivity of the copper electrodes $\rho_{electrodes} = 1.72 \cdot 10^{-8}$ Ωm in all cases.

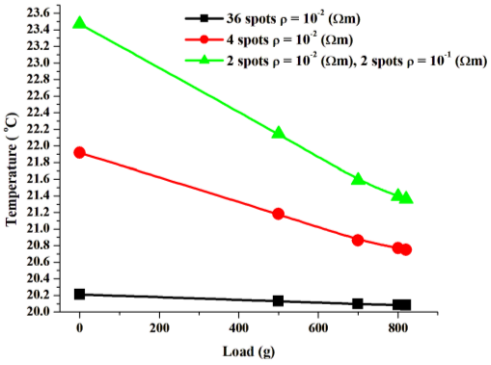

Fig. 5.21. Temperature variation against contact load (ST: 1 µm): (a) 36 spots ($\rho_{ZrCuspots} = 1 \cdot 10^{-2}$ Ωm); (b) 4 spots ($\rho_{ZrCuspots} = 1 \cdot 10^{-2}$ Ωm); (c) 4 spots (2 spots ($\rho_{ZrCuspots} = 1 \cdot 10^{-2}$ Ωm); 2 spots ($\rho_{ZrCuspots} = 1 \cdot 10^{-1}$ Ωm)).

5.2.3.1.2. Electro-Thermal Analysis (Contact Spot Thickness of 10 µm)

Fig. 5.22 shows the steady-state temperature distribution vs contact load for a spot thickness of 10 µm with: (a) 36 spots ($\rho_{ZrCuspots} = 1 \cdot 10^{-2}$ Ωm); (b) 4 spots ($\rho_{ZrCuspots} = 1 \cdot 10^{-2}$ Ωm); (c) 4 spots (2 spots ($\rho_{ZrCuspots} = 1 \cdot 10^{-2}$ Ωm) and 2 (spots $\rho_{ZrCuspots} = 1 \cdot 10^{-1}$ Ωm)) with the resistivity of the copper electrodes $\rho_{electrodes} = 1.72 \cdot 10^{-8}$ Ωm in all cases.

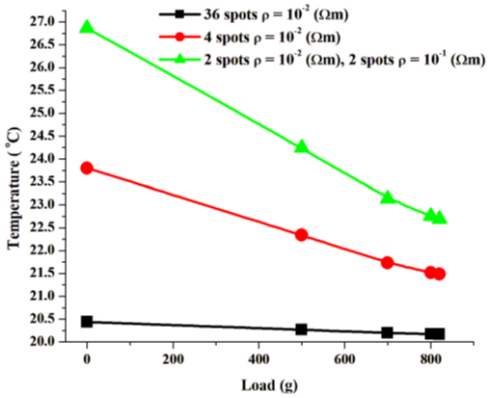

Fig. 5.22. Temperature variation against contact load (ST: 10 µm): (a) 36 spots ($\rho_{ZrCuspots} = 1 \cdot 10^{-2}$ Ωm); (b) 4 spots ($\rho_{ZrCuspots} = 1 \cdot 10^{-2}$ Ωm); (c) 4 spots (2 spots ($\rho_{ZrCuspots} = 1 \cdot 10^{-2}$ Ωm) and 2 spots ($\rho_{ZrCuspots} = 1 \cdot 10^{-1}$ Ωm)).

5.2.3.1.3. Electro-Thermal Analysis (Contact Spot Thickness of 13 µm)

Fig. 5.23 provides the electrical contact model's steady-state temperature against the contact load with a spot thickness of 13 µm for: (a) 36 spots ($\rho_{ZrCuspots} = 1 \cdot 10^{-2}$ Ωm); (b) 4 spots ($\rho_{ZrCuspots} = 1 \cdot 10^{-2}$ Ωm); (c) 4 spots (2 spots ($\rho_{ZrCuspots} = 1 \cdot 10^{-2}$ Ωm) and 2 (spots $\rho_{ZrCuspots} = 1 \cdot 10^{-1}$ Ωm)), with the resistivity of the copper electrodes $\rho_{electrodes} = 1.72 \cdot 10^{-8}$ Ωm in all cases.

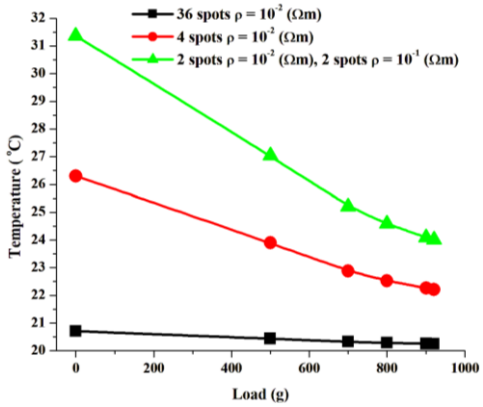

Fig. 5.23. Temperature variation against contact load (ST: 13 µm): (a) 36 spots ($\rho_{ZrCuspots} = 1 \cdot 10^{-2}$ Ωm); (b) 4 spots ($\rho_{ZrCuspots} = 1 \cdot 10^{-2}$ Ωm); (c) 4 spots (2 spots ($\rho_{ZrCuspots} = 1 \cdot 10^{-2}$ Ωm) and 2 spots ($\rho_{ZrCuspots} = 1 \cdot 10^{-1}$ Ωm)).

5.2.4. Discussion

The study examines the contact resistance of copper electrodes connected by ZrCu contact spots, using numerical and analytical methods, and analyzing the temperature distribution. The Multiphysics evaluation demonstrates that contact resistance varies between 7 mΩ (ST: 13 μm) and 0.8 mΩ (ST: 1 μm) for an unaged contact under normal conditions. The analytical solutions show higher resistance values than those obtained numerically, all values are expressed in [mΩ] according to IEC standards (IEC-512-2-2a).

Fig 5.17-5.19 shows the effect of aging on contact resistance. As expected, the contact resistance increases with the resistivity of the ZrCu spots on the surface and decreases when the value of the applied load increases; similar characteristics of the contact resistance as a function of the applied load were also observed in Fig 5.6-5.8. Although the simulated maximum temperature in Fig. 5.21-5.23 was 23.5 ˚C, 26.9 ˚C, and 31.5 ˚C, respectively, this temperature can increase rapidly in the presence of aging factors in electrical contact operating environments, such as near a vehicle engine.

CHAPTER 6 - EXPERIMENTAL VALIDATION OF CONTACT RESISTANCE CALCULATION

This chapter presents the experimental analysis of the contact resistance calculation and aims to validate the numerical results obtained in Model IV and the analysis of electrical connection deterioration by performing accelerated thermal aging on contact samples fabricated by vacuum deposition of a ZrCu alloy using cathodic arc deposition equipment. Contact resistance was evaluated using a four-probe measurement technique and a Keithley multimeter under normal temperature and pressure conditions.

6.1. Samples

The two contact electrodes are made of copper-clad laminate (CCL) and one of them has ZrCu spots deposited on it to emulate a real (imperfect) contact. A mask made of a 36-hole circuit board (PCB) was used to deposit the spots on the lower electrode, the size and shape of the spots being given by the PCB, as in Fig. 6.1.

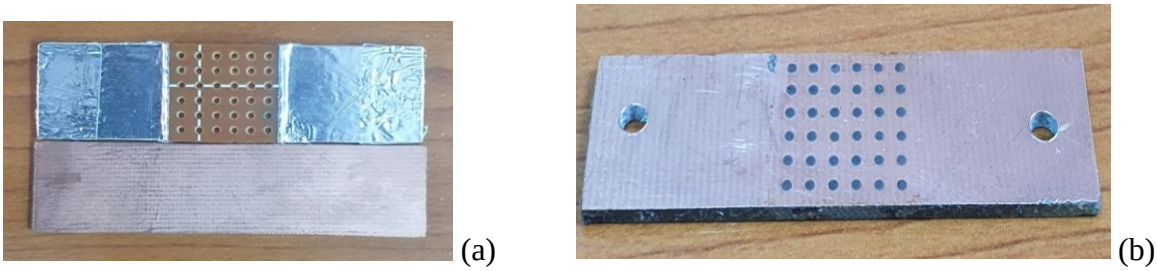

Fig. 6.1. Contact sample: (a) before deposition; (b) after deposition of ZrCu coatings spots.

A cathodic arc deposition machine with a single cathode constructed of ZrCu alloy (50 percent Zr, 50 percent Cu, 99.9 percent purity) provided by Cathay Advanced Materials Limited was used to create the ZrCu-based coatings. The deposition time was varied between 20 and 100 minutes to achieve different coating thicknesses ranging from 1 to 13 µm. Fig. 6.2 illustrates the coating thickness obtained for a thickness of 1 µm.

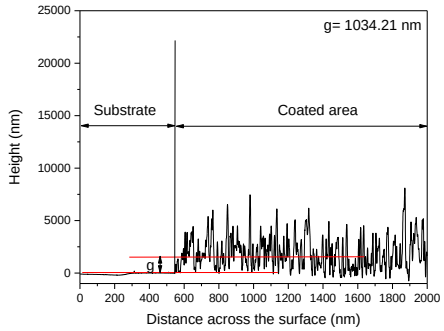

Fig. 6.2. Thickness of the coatings in a randomly selected zone.

6.2. Experimental Setup and Measurements

This thesis used a four-wire resistance measuring technique to experimentally determine the contact resistance using a Keithley 2700 multimeter, with a maximum current of 10 mA (Fig 6.3).

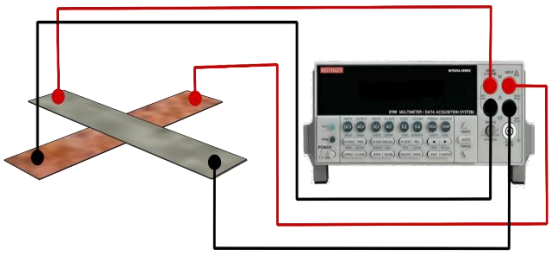

Fig. 6.3. Keithley multimeter four-wire resistance measurement.

To measure the contact resistance, an assembly consisting of two electrodes placed in a cross-shape was used, over which weights of 500, 700, 800, 820, 900, and 920g respectively were applied as in Fig. 6.4. After evaluation of the initial resistance, thermal

aging was carried out in a forced air oven for 277 hours at 50°C (Fig. 6.5). All contact resistance determinations were carried out at room temperature, without housing.

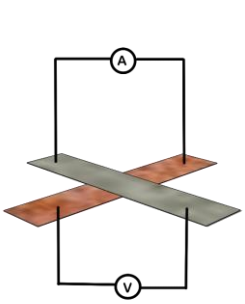

(a)

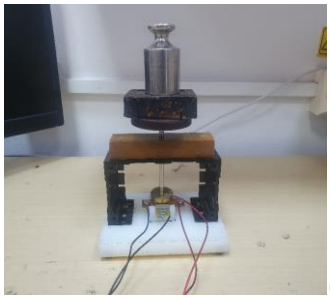

(b)

Fig. 6.4. Experiment set to determine contact resistance: (a) Diagram of a four-point probe circuit, (b) measuring assembly with weights placed to increase contact force.

Fig. 6.5. Aged contact samples in the presence of sodium chloride (NaCl) solution in a forced-air oven.

The accelerated thermal aging and contact resistance measurement procedure involves setting up contact samples, measuring the initial resistance for different positions of the applied loads using the Keithley 2700 multimeter, then placing them in a forced-air oven for 277 hours, and taking contact resistance measurements at 42-hour intervals. Experiments were performed on contact samples with deposition thicknesses of 1 μm, 10 μm, and 13 μm, respectively.

6.3. Experimental Results

6.3.1. Contact Sample with ZrCu Alloy Spot Deposition of 1 μm

The contact resistance values were acquired by positioning the load on the measurement platform in various positions (randomly, back, right, center, front, left) and at various aging periods. For each aging period (0 - 277 hrs), the study revealed a mixed trend in contact resistance as aging time increased, with a decrease and increase observed in aging time 0 to 86 hours and an increase in 126-277 hours, possibly due to contact-resistant measurements not being made at the same spot for every measurement. Overall, heat stress

hastens the aging of electrical connections. Fig. 6.6a-f shows the contact resistance measurements obtained for all positions as a function of the force applied on the measurement assembly platform.

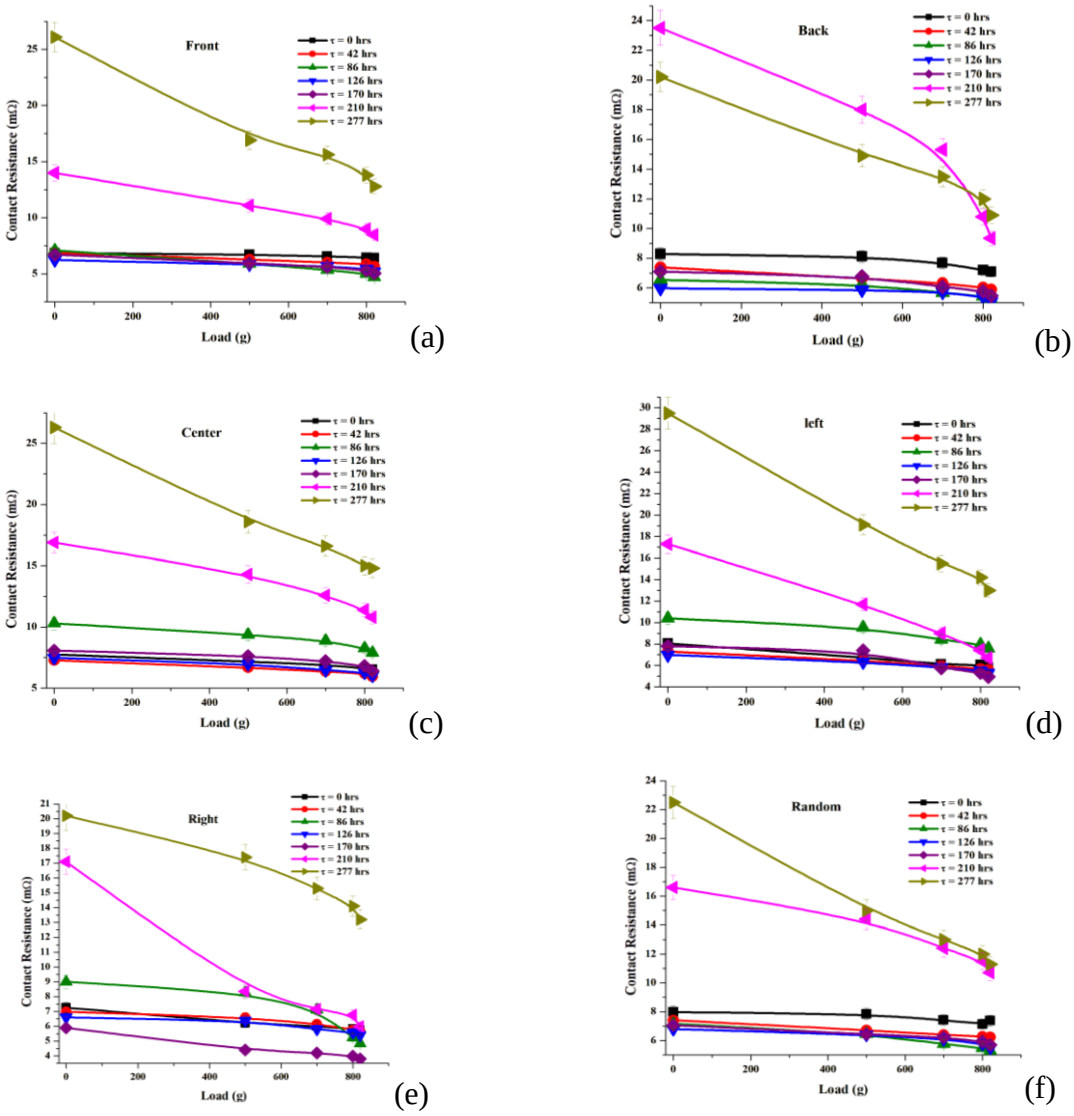

Fig. 6.6. Contact resistance against contact load for different positions of applied force measured for different aging times (DT: 1 µm): (a) front, (b) back, (c) center, (d) left, (e) right, (f) random.

For a clear and concise analysis, the contact resistance measured for all positions was averaged and presented in Table 6.1 and Fig 6.7. It shows that contact resistance increases with aging time and is influenced by contact load, with contact resistance decreasing as contact load increases due to a rise in the actual contact area at the electrical contact sample's interface.

Table 6.1.

Average Contact Resistance Values Measured for Different Points of Applied Force (DT: 1 µm).

***Aging time* (hrs)**	***Load* (g)**					-
	0	500	700	800	820	
0	7.70	7.14	6.78	6.55	6.50	***Contact Resistance (mΩ)***
86	8.41	7.63	6.87	6.23	5.92	
210	17.6	13	11.1	9.47	8.66	
277	24.1	17	14.9	13.5	12.7	

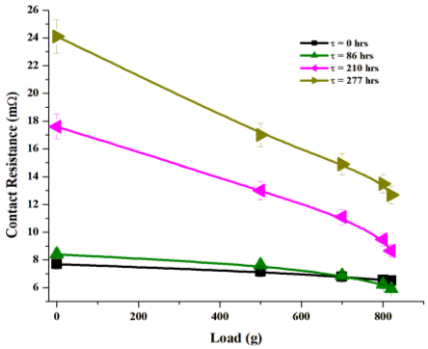

Fig. 6.7. Contact resistance versus contact load determined by averaging data obtained at several applied force points (DT: 1 µm).

Fig. 6.8 demonstrates that contact resistance increases with aging time, influenced by impurities and environmental conditions. Increased contact resistance can lead to damage and eventual failure of electrical contacts.

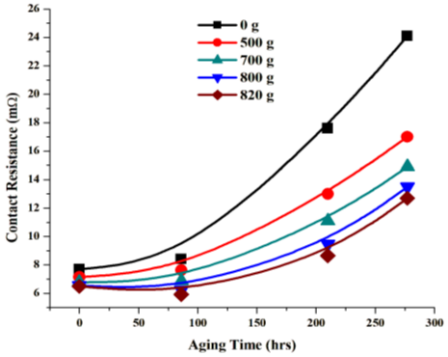

Fig. 6.8. Change in contact resistance against aging time (DT: 1 µm).

6.3.2. Contact Sample with ZrCu Alloy Spot Deposition of 10 µm

The contact resistance of a sample with 10 µm thick ZrCu alloy coatings was evaluated at various positions and averaged to obtain the final value. Table 6.2 and Fig 6.9 illustrates the average contact resistance values.

Table 6.2.

Average Contact Resistance Values Measured for Different Points of Applied Force (DT: 10 µm)

***Aging time* (hrs)**	***Load* (g)**					-
	0	500	700	800	820	
0	9.16	7.59	7.32	7.12	7	***Contact Resistance (mΩ)***
42	11.5	9.25	8.28	7.89	7.61	
170	15.2	12.4	11.5	11.2	11	
210	15.7	12.4	11.5	10.8	10.3	
277	37.6	26	22.6	20.4	19.5	

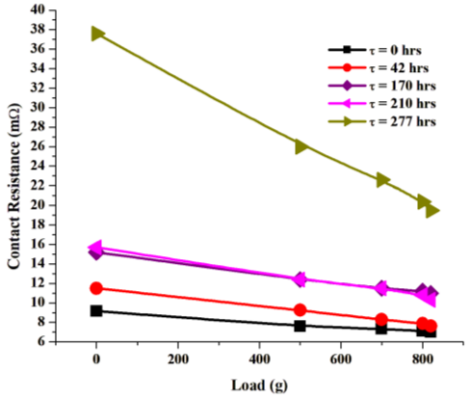

Fig. 6.9. Contact resistance versus contact load determined by averaging data obtained at several applied force points (DT: 10 µm).

Fig 6.10 shows the contact resistance's increase over time due to oxidation, contamination, roughness, and wear on contact surfaces. This is particularly true for corrosion-prone metals and harsh environmental conditions. Over time, these elements may result in a gradual rise in resistance.

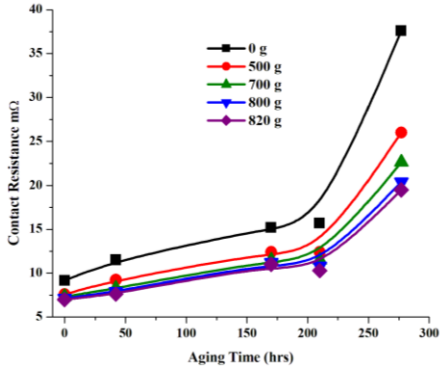

Fig. 6.10. Change in contact resistance against aging time (DT: 10 µm).

6.3.3. Contact Sample with ZrCu Alloy Spot Deposition of 13 µm

Five samples (I, II, III, IV, and V) were analyzed for the calculation of contact resistance with ZrCu deposition thickness of 13 µm. Table 6.3 and Fig. 6.11 show the average contact resistance values of sample III as it ages over time with different applied loads. The contact resistance is displayed in Fig. 6.12 as a function of aging time. In line with expectations, contact resistance rises as aging time increases in all cases.

Table 6.3.

Average Contact Resistance Values Measured for Different Points of Applied Force (Sample III)

***Aging time* (hrs)**	***Load* (g)**						-
	0	500	700	800	900	920	
0	11.5	11	10.6	10.3	9.91	9.75	***Contact Resistance (mΩ)***
42	50.7	43.8	37.5	34.1	31.4	30.5	
86	85.6	77.4	72.9	68.2	62.6	60.9	
210	156	131	116	107	101	95.3	
277	588	445	388	360	311	285	

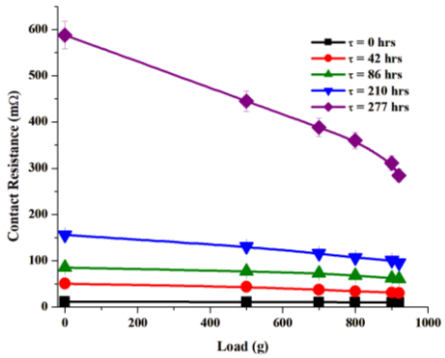

Fig. 6.11. Contact resistance versus contact load determined by averaging data obtained at several applied force points (Sample III).

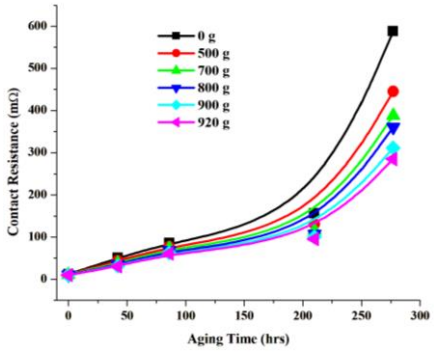

Fig. 6.12. Change in contact resistance against aging time (Sample III).

6.4. Discussion

The experimental studies validate Model IV and investigate changes in electrical resistance of fabricated electrical contact samples. Copper clad laminate (CCL) was used to fabricate these samples, and spots of ZrCu (an alloy with higher resistivity than copper) with thicknesses of 1 μm, 10 μm, and 13 μm, respectively, were deposited on the surface of one of the two-component electrodes to emulate a real (imperfect) contact. To study the long-term effects, accelerated thermal aging was carried out using a forces flow oven. The study aims to characterize electrical contacts and the impact of external influences like temperature on contact resistance changes. The experiment was carried out on the following:

- A contact sample having 1 μm deposition thickness;
- A contact sample having 10 μm deposition thickness;
- Five contact samples having 13 μm deposition thickness (Samples I - V).

The study used a four-point resistance measurement method to determine contact resistance values for all contact samples. The load was placed in various locations on the measuring platform for different aging times (0-277 hours). These values were averaged in all cases for a better and more detailed analysis of the variance in the contact resistance of the fabricated samples. The results showed that the contact resistance decreases as the applied load increases.

Although measurements were made at room temperature with controlled load application and measured constantly, the relationship between contact resistance and aging time for all applied load positions has a variable increasing and decreasing trend. This is due to differences in contact points between electrodes and physical changes in the material or component over time. Variations in load applied to the material or component also contribute to contact resistance variations. Despite these changes, the average contact resistance against aging time results shows that aging mechanisms like temperature, humidity, and oxide films deteriorate electrical contacts by increasing contact resistance, ultimately leading to failure.

In Chapter 5, a numerical analysis was implemented on Model IV, and contact resistance was simulated as a function of applied load for an unaged electrical contact with a spot thickness (ST) of 1 μm, 10 μm, and 13 μm, respectively. As illustrated in Fig. 6.13, the numerical results are compared with the corresponding experimental results.

At a contact load of 0 g – 800 g, for spot thickness of 1 μm, the contact resistance ranges from 7.7 mΩ to 6.5 mΩ (experimental) and 2 mΩ - 0.8 mΩ (numerical); 9 mΩ - 7 mΩ

(experimental) and 4 mΩ - 1.5 mΩ (numerical) for spot thickness of 10 µm; 11.5 mΩ - 9.8 mΩ (experimental) and 7 mΩ - 2.8 mΩ (numerical) for spot thickness of 13 µm.

The comparison between numerical and experimental analysis shows agreement in various aspects, including curves and contact resistance. Both studies yield results in the order of magnitude of mΩ. As contact load improves, contact resistance drops. However, experimental values for contact resistance are higher than numerical analysis values due to rough surfaces with numerous asperities in ZrCu spots, making it difficult to make contact at the same point for every measurement.

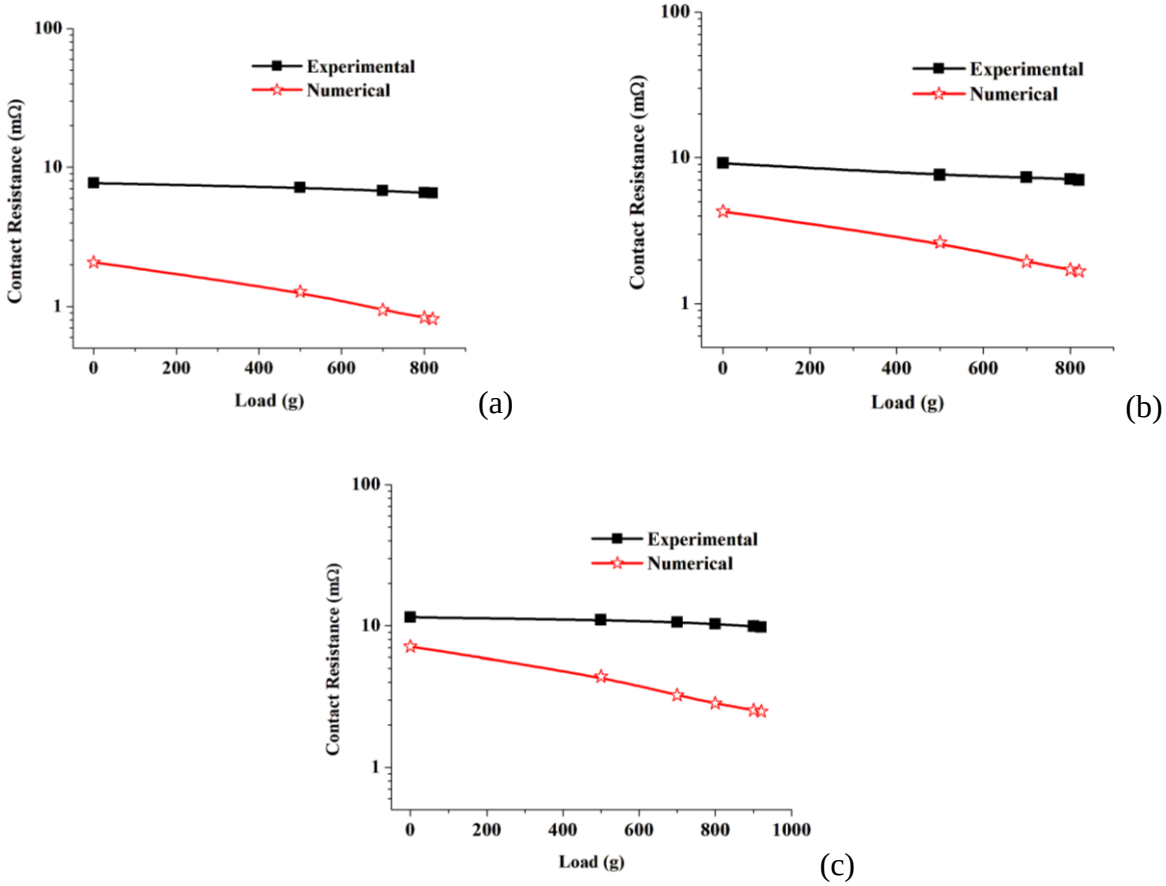

Fig. 6.13. Contact resistance versus the contact load for ZrCu spots thickness of 1 µm (a); 10 µm (b); 13 µm (c) obtained numerically and experimentally.

The results in Fig. 6.13 validate the numerical models from an electrical perspective, making them reliable for studying the thermal regime. This means that the thermal regime obtained exclusively through numerical modeling is reliable and trusted for estimating thermal characteristics.

GENERAL CONCLUSION, ORIGINAL CONTRIBUTIONS, AND FUTURE WORK

General Conclusion

This thesis addressed the degradation of low-current electrical contact due to aging factors using numerical, analytical, and experimental analysis. Chapters 3, 4, and 5 presented numerical and analytical analysis, while Chapter 6 focused on the experimental aspect.

Chapter 3 proposes four models (Model I - IV) for numerical analysis in the thesis, focusing on the physical, geometrical, mathematical, and discretization of computational domains, highlighting the development and presentation of these models.

Chapter 4 presents the Multiphysics (electro-thermal) analysis carried out on Model I and Model II, which was done in the electro-kinetic regime. It is shown that temperature variation has no significant effect on thermal conductivity. The effects of aging factors such as oxide films, current, and temperature on the degradation process of electrical contact were analyzed in both models, and it was concluded that the presence of oxide films at the contact interface increases the temperature. Also, the temperature increases as the thickness of the oxide film and the electric current increases. Moreso, it was observed that the temperature was more pronounced at the interface in the contact zone. This Multiphysics analysis elaborated a detailed picture of the degradation process that occurs in low-current and how all these factors in practice can fasten the deterioration of electrical connectors over time.

Since contact resistance is the main criterion for determining the state of an electric contact, Chapter 5 focuses on the numerical (Multiphysics) and analytical calculation of contact resistance. This objective was achieved using Model III and Model IV, considering the nature and characteristics of the spots at the interface. In this sense, the variation of contact resistance of the contact spots with spot radius (in Model III) and contact load (Model IV) was analyzed both numerically and analytically. The numerical analysis was done by obtaining the voltage drop across the contact spots at the interface of the contact model, and the contact resistance was calculated using Ohm’s law. Regardless of the model used, it was observed that the contact resistance depends on the actual contact area of the electrical connector asperities, i.e., the actual contact area increases with the applied load, which ultimately improves the contact resistance. Furthermore, thermal analysis was not possible analytically; only numerical modeling was the best solution. The influence of aging on the contact resistance of low-current connectors showed that contact resistance increases and leads to an increase in temperature which promotes and accelerates the degradation process.

Though the developed numerical models presented in this thesis were simplified models, the results presented in this thesis indicate the severity of damage electrical contacts can obtain due to the activities of degrading factors like oxide films, temperature, current, etc.

In Chapter 6, contact samples were fabricated using the cathodic arc deposition technique. The samples were prepared based on the specifications of Model IV to validate the numerical model. The contact resistance was evaluated using the four-point probe contact resistance measurement. To validate the numerical model, the contact resistance result obtained numerically for Model IV was compared to that obtained experimentally. It was observed that both numerical and experimental curves for contact resistance as a function of applied load were similar in the order of mΩ, thus validating the numerical results. The contact resistance values for the experimental analysis were higher than those of the numerical analysis in all cases; this is due to small variations in the placement of the samples in the measurement assembly used for the experimental determinations.

Original Contributions

- The thesis was carried out by doing elaborate documentation on the aging of electrical contacts, which occurs as a result of numerous aging factors (temperature, oxide films, etc.), and highlighting the effect they have on contact resistance.
- Development of numerical models with different configurations and applying a Multiphysics study to study the electro-mechanical and thermal field of the contact models using the finite element method in the electro-kinetic regime.
- Carrying out complex aging analysis on the developed numerical models by considering different degradation states of the models (presence of oxide films, an increase of current, thickness of the oxide films at the interface, variation of electrical conductivity with temperature, increase, and decrease of the true area of contact, application of contact load).
- Performing analytical calculations to evaluate the contact resistance considering the multi-spot contact model, as well as numerical evaluation of contact resistance
- Detailed comparison between the contact resistance results of analytical models and numerical models. Further analysis was done by highlighting the influence of aging on contact resistance and the thermal field.
- Fabrication of electrical contact samples by cathodic arc deposition and defining the characterization, composition, thickness, morphology, and roughness of the deposited coatings.

- Experimental determination of contact resistance and the thermal aging process of the fabricated contact samples using the four-point probe resistance measurement method and forces-flow oven, respectively. The measurement of the contact resistance of the samples was achieved by creating a measuring assembly to adapt the contact samples and the applied contact loads for measurement.
- Experimental studies on the influence of accelerated aging (thermal aging in the presence of sodium chloride solutions at 50 ºC) and applied load on contact resistance.
- Data processing for both numerical and experimental analysis for different samples and graphical representation of all findings, which puts in evidence the influence of aging mechanisms on electrical contacts and a good correlation between experimental results and the numerical predictions.

Future Work

Based on the accomplished studies in the present Ph.D. thesis, the following perspective on future work is proposed:

- Improve the present numerical models from the point of view of geometry by developing and incorporating contact models into contact housing and analyzing different contact materials. From the point of view of simplifying the hypothesis, by defining a well-structured Multiphysics problem considering the impact of convection and radiation mechanism, vibration on the aging of electrical contacts.
- Study the aspects regarding electrical contact cables used in low-level current applications and the role they play in the degradation process of electrical contacts.

REFERENCES

[1.1]. 2016-11_Imagebroschuere_Steckverbinder_engl.pdf

[2.1]. Braunovic, Milenko. (2007). Reliability of power connections. Journal of Zhejiang University: Science A: Applied Physics & Engineering, 8. 343 – 356 doi:10.1631/jzus.2007.A0343.

[2.2]. Braunovic. M, Myshkin, Nikolai K, Konchits, Valery. V, "Electrical Contacts: Fundamentals, Applications, and Technology." *CRC Press; 1st edition* (December 15, 2006).

[2.3]. Weißenfels, Christian and Wriggers, Peter. (2010). "Numerical modeling of electrical contacts." *Computational Mechanics*. *46. 301-314*, doi:10.1007/s00466-009-0454-8.

[2.4]. Holm, R. "Electric Contacts Theory and Application," *4th ed.; Springer: Berlin/Heidelberg*, Germany, 1967.

[2.5]. J. A. Greenwood, "Constriction Resistance and the Real Area of Contact," *Brit. J. Appl. Phys*., vol. 17, pp. 1621-1632, 1966.

[3.1]. G.-G. Dankat, A.-A. Dobre, and L.-M. Dumitran, "Numerical Simulation of Thermal Condition of a Low Current Electric Contact: n/a", *Electric Machines, Materials and Drives- Present and Trends*, vol. 16, no. 1, pp. 53–61, Jan. 2020.

[3.2]. https://www.azonano.com/article.aspx?ArticleID=3395

[3.3]. Liu, M., Lin, M.C. & Wang, C, "Enhancements of thermal conductivities with Cu, CuO, and carbon nanotube nanofluids and application of MWNT/water nanofluid on a water chiller system". *Nanoscale Research Letters 6*, no. 297, 2011.

[3.4]. G. G. Dankat, A. A. Dobre and L. M. Dumitran, "Influence of Ageing on Electrothermal Condition of Low Current Contact," *2021 12th International Symposium on Advanced Topics in Electrical Engineering (ATEE)*, 2021, pp. 1-6, doi: 10.1109/ATEE52255.2021.9425242.

[3.5]. Dankat, Gideon Gwanzuwang, and Laurentiu Marius Dumitran. 2022. "Computation of the Electrical Resistance of a Low Current Multi-Spot Contact" *Materials 15, no. 6: 2056*. https://doi.org/10.3390/ma15062056.

[3.6]. Lee, Ching-Jen & Lin, Hsuan-Kai & Sun, S. & Huang, Jacob. (2010). Characteristic difference between ITO/ZrCu and ITO/Ag bi-layer films as transparent electrodes deposited on PET substrate. *Applied Surface Science - APPL SURF SCI*. 257. 239-243. 10.1016/j.apsusc.2010.06.074.

[3.7]. Filippov, V & Yagodin, Denis & Shunyaev, K & Leont'ev, L. (2018). Electrical Resistivity of Cu-Zr Melts. Doklady Physical Chemistry. 483. 155-158. Doi:10.1134/s0012501618120035.

[4.1]. G.-G. Dankat, A.-A. Dobre, and L.-M. Dumitran, "Numerical Simulation of Thermal Condition of a Low Current Electric Contact: n/a", *Electric Machines, Materials and Drives- Present and Trends*, vol. 16, no. 1, pp. 53–61, Jan. 2020.

[4.2]. G. G. Dankat, A. A. Dobre and L. M. Dumitran, "Influence of Ageing on Electrothermal Condition of Low Current Contact," *2021 12th International Symposium on Advanced Topics in Electrical Engineering (ATEE)*, 2021, pp. 1-6, doi: 10.1109/ATEE52255.2021.9425242.

[5.1]. G.-G. Dankat, A.-A. Dobre, and L.-M. Dumitran, “Analytical and Numerical Computation of Electrical Resistance in a Low Current Multi-Spots Metallic Contact”, Electric Machines, Materials and Drives- Present and Trends, vol. 17, no. 1, pp. 52–59, Feb. 2022.

[5.2]. Dankat, Gideon Gwanzuwang, and Laurentiu Marius Dumitran. 2022. "Computation of the Electrical Resistance of a Low Current Multi-Spot Contact" *Materials 15, no. 6: 2056*. https://doi.org/10.3390/ma15062056.

[5.3]. Wang Shujuan, Hu Fang, Su Bonan, and Zhai Guofu, "Method for calculation of contact resistance and finite element simulation of contact temperature rise based on rough surface contact model," *26th International Conference on Electrical Contacts (ICEC 2012)*, 2012, pp. 317-321, doi: 10.1049/cp.2012.0668.

[5.4]. Y. Shibata et al., "Detailed analysis of contact resistance of fretting corrosion track for the tin-plated contacts," *26th International Conference on Electrical Contacts (ICEC 2012)*, 2012, pp. 228-232, DOI: 10.1049/cp.2012.0652.

[5.5]. P.G. Slade, *Electrical Contacts: Principles and Applications*, 2nd ed. CRC Press, pp 375 - 384 2014.

[5.6]. P. Lindholm, "Numerical Study of Asperity Distribution in an Electrical Contact," *2011 IEEE 57th Holm Conference on Electrical Contacts (Holm)*, Minneapolis, MN, USA, 2011, pp. 1-5, doi: 10.1109/HOLM.2011.6034796.

[5.7]. Junxing Chen, Mingzhe Rong, Fei Yang, Yi Wu, Hao Sun, and Yun Yang, "Numerical research on the electrical contact model and thermal analysis of the Roll-Ring," *2013 2nd International Conference on Electric Power Equipment - Switching Technology (ICEPE-ST)*, Matsue, Japan, 2013, pp. 1-4, doi: 10.1109/ICEPE-ST.2013.6804345.

[5.8]. T. Kondo, H. Nakata, J. Sekikawa, Y. Kubota, K. Hayakawa, and T. Nakamura, "An analysis of the relationship between contact resistance and fracture of oxide film for connector contacts using finite element method," *2014 IEEE 60th Holm Conference on Electrical Contacts (Holm)*, New Orleans, LA, USA, 2014, pp. 1-6, doi: 10.1109/HOLM.2014.7031025.